

DELFT UNIVERSITY OF TECHNOLOGY

MEP AP3902MTP
RST DEPARTMENT, MP&T SECTION

**Adjoint Method for Beam Angle
Selection in Radiotherapy**

Joshua van den Bos (4593405)

Supervisors:

Zoltán Perkó and Danny Lathouwers

April 29, 2021



Abstract

Radiotherapy is one of the main methods to treat cancer. While photons are still the most common used particles in external beam radiotherapy, protontherapy is becoming more and more popular. The main advantage of protons compared to photons is their dose deposition. The dose deposition of protons follows a Bragg-peak, which leads to more locally deposited dose and spares more healthy tissue. On the other hand, protons are more sensitive for uncertainties.

Even more healthy tissue can be spared, when irradiating the tumor cells from optimal angles. Organs might be avoided, or shorter paths through the body are possible, for example. However, choosing the optimal set of beam angles for a specific case is difficult and often done manually.

In this thesis, a new methodology called the adjoint method is developed to select an optimal set of beam angles and beam weights in external beam radiotherapy. The Linear Boltzmann Transport Equation is specifically adjusted for proton transport and forms the Fokker-Planck approximation. The Fokker-Planck approximation models proton transport. Only the continuous slowing down operator, the straggling operator and a source are considered in the approximation. Numerical analysis is performed to solve the Fokker-Planck approximation. The discretization of the energy domain is done with the Discontinuous Galerkin method, and ray-tracing of beams in the spatial domain is done with the Crank-Nicolson method.

A minimum least squares objective function is introduced to find the optimal selection of beam angles. The gradient descent method is applied to find a local minimum of the objective function. The gradient is calculated by performing adjoint transport of protons. Adjoint transport is based on an adjoint source, which is changing every iteration based on the dose deposition. The dose deposition is computed using forward transport of protons and uses the newest optimization variables. This way, several iterations can be performed.

The algorithm works well for a small and simple set-up. Two beam directions were possible: \hat{x} and $-\hat{x}$. 77 iterations are performed in 290 seconds and a possible local minimum is achieved. The stepsize tolerance limit is reached. The objective value decreased from $1.728 \cdot 10^6$ to $8.12 \cdot 10^4$. The tumor nearly receives the prescribed dose, while organs are mostly avoided. The flux input of the beams and the gradient are in good agreement with the dose distribution and energy is conserved.

More possible beam directions do not lead to a better result. Although possible local minimums are achieved, - the stepsize tolerance limit is reached - the objective value and the computation time increase. The number of optimization variables also increased, which could have led to extra difficulties for the solver to find the optimal values. Future research should investigate and solve the problems for large systems.

Acknowledgements

Due to the coronavirus, everything is different. Nevertheless, I was still able to complete my thesis within reasonable time. However, this would not be possible without the help of some people. First, I want to thank Zoltán Perkó for making this project possible. His ideas and valuable feedback have been very important to lead this research to a succesful end. Second, I want to thank Danny Lathouwers for providing insight in some important coding aspects. Both were always open to questions and I appreciate the smooth connection with them (even though we only had online meetings). Finally, I want to thank my family for the immense support they gave me during all those months.

Contents

Abstract	iii
Acknowledgements	vi
1 Introduction	1
1.1 Cancer and radiotherapy	1
1.2 Proton therapy	2
1.3 Particle transport	3
1.3.1 Forward transport	3
1.3.2 Adjoint transport	5
1.4 Goal of this research	6
1.5 Thesis outline	7
2 Proton transport	8
2.1 Linear Boltzmann Transport Equation	8
2.2 Fokker-Planck approximation	9
2.3 Discretization	12
2.3.1 Energy domain - Discountinuous Galerkin	12
2.3.2 Continuous Slowing Down operator	14
2.3.3 Straggling operator	16
2.3.4 Spatial domain - Crank-Nicolson	17
2.3.5 Boundary conditions	18
2.4 Dose calculation and discretization	19
3 Adjoint method	22
3.1 Adjoint Fokker-Planck approximation	22
3.2 Perturbation analysis	25
3.3 Adjoint source formulation	26
3.4 Gradient descent optimization	28
3.5 Adjoint discretization	31
3.5.1 Adjoint Continuous Slowing Down operator	31
3.5.2 Adjoint Straggling operator	33
3.5.3 Adjoint source	34
3.5.4 Crank-Nicolson - adjoint	34
3.6 Beam angle selection	35
4 Results	38
4.1 Set-up	38
4.2 Validation	43
4.3 Objective function	45

4.4	Dose distribution	46
4.5	Forward flux	47
4.6	Influence of direction	51
5	Conclusion and Recommendations	55
5.1	Conclusion	55
5.2	Recommendations	55
	References	57

1 Introduction

The motivation and background for this research are explained in this chapter. The basics about proton therapy, forward transport, and adjoint transport are described. The goal of this research and the research question are stated as well. The thesis outline is given at the end of this chapter.

1.1 Cancer and radiotherapy

Cancer is a very common disease and causes the second most deaths worldwide. It is the cause of every sixth death. Since 1990, the number of cancer deaths has increased by 66% and the death rate from cancer is increased by 17%. However, the death rate from cancer has declined by 15%, if the age structure of the population had stayed the same over time and would be the same across countries [17]. This decrease is caused by treatments such as surgery, chemotherapy and radiotherapy. In 2018, 18.1 million new cases and 9.5 million cancer-related deaths were registered worldwide. In 2040, the number of new cancer cases and the number of cancer-related deaths per year are expected to rise to 29.5 million and 16.4 million respectively [22]. The main reasons for this increase are the growing world population and aging. Improving treatments such as radiotherapy is one of the better diagnostics to reduce the number of deaths significantly in future.

In radiotherapy, patients are treated by (ionizing) irradiation to eliminate tumor cells. Various types of radiotherapy exist of which external beam radiotherapy is the most common. In external beam radiotherapy, a number of beams have fixed positions around the patient in a 2π circle or a 4π sphere. Another option is to move a single beam around the patient in a circular or spiral shape [2].

Intensity-modulated radiation therapy (IMRT) is an advanced type of high precision radiation. It modulates the intensity of the incoming photon or proton beams conform to the shape of a tumor. This added flexibility (compared to conventional beams of uniform intensity) can be utilized to achieve a better homogeneous dose distribution within the tumor target volume [8].

A linear accelerator is located within the gantry to generate a high energy radiation beam for therapy. This high energy radiation beam may be a photon (X-ray) beam or a proton beam [6]. This beam delivers a dose of photons or protons to irradiate tumor cells in the patient. However, the photons or protons first travel through healthy tissue before reaching the tumor cells. Therefore, they deposit a part of their dose in healthy tissue

due to interactions. This dose deposition in healthy tissue is unwanted and by choosing an optimal set of beam angles with optimal beam weights to treat the patient, the dose to healthy tissue can be minimized, while the tumor cells still receive the prescribed dose. Developing an algorithm to choose the optimal beam angle selection for external beam radiotherapy is the topic of this research.

1.2 Proton therapy

As stated in Section 1.1, photons or protons can be used to eliminate tumor cells. In this study, protons will be used instead of photons, because protons have a major advantage in dose deposition. While the distribution of the photon dose is over the complete distance they travel, the distribution of the proton dose contains a Bragg peak, as shown in Figure 1.

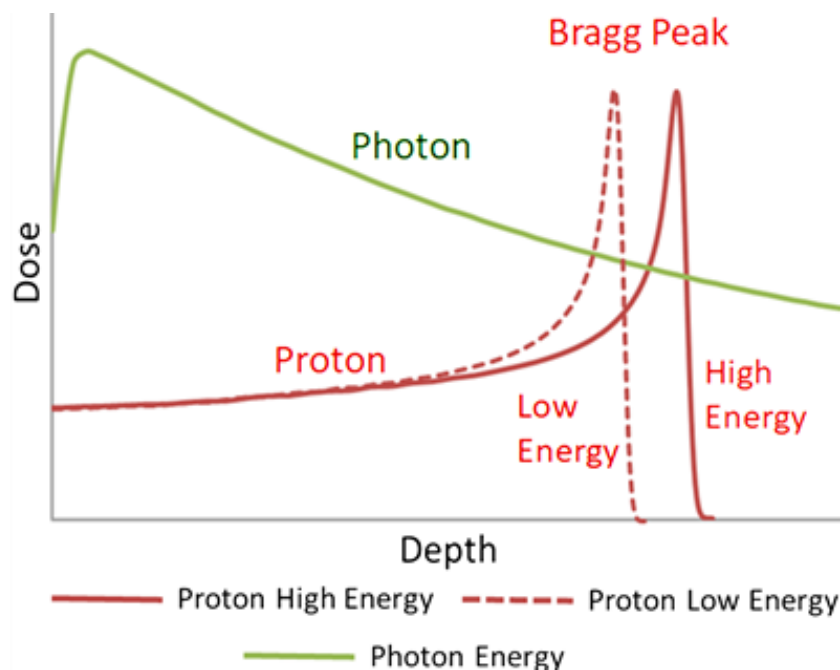


Figure 1: Illustration of the dose deposition for photons and protons. Photons deposit a part of their energy (dose) at every depth, while protons have a peak deposition at a specific depth for a specific energy [16].

This proton distribution allows to lower the dose in unwanted areas such as organs at risk (OAR) and normal tissue, especially when they are located behind the tumor. The dose in the tumor is not affected. Beams with

a different initial energy have their Bragg peaks at different depths, since protons with higher initial energy can travel further into the medium. When multiple Bragg peaks at different energy levels (pristine peaks) are combined, a spread-out Bragg peak (SOBP) is formed to cover the tumor uniformly [10].

Treatment plans are made to eliminate a tumor in the best possible way. These plans contain parameters such as the location of tumor cells, the locations of organs, and the desired tumor dose. A computed tomography (CT) scan of the patient determines the locations of tumors and organs. The desired dose depends on the kind of tumor. Based on the treatment plan, an optimal set of beam angles can be chosen to irradiate the patient with minimal organ and tissue damage, while tumor cells still get irradiated by the prescribed dose.

However, there also is a major disadvantage when using protons compared to photons. Errors may occur in the prediction of the range of the protons, or the CT scan is not completely accurate due to movement by the patient during measurements of the tumor and organ locations [7]. These errors can cause more damage when protons are used instead of photons, since a peak dose might be deposited in an unwanted area.

1.3 Particle transport

Particle transport can be used to determine an optimal beam angle selection. Forward and adjoint transport are the two main approaches of particle transport. Both approaches apply ray-tracing through the phantom, but they differ in their approach. In Sections 1.3.1 and 1.3.2, forward transport and adjoint transport are described, respectively.

1.3.1 Forward transport

In forward transport, one starts with a predefined selection of beams. These beams are often located at equally spaced distances from each other around the patient. The intensity and the direction of the beams can be adjusted to minimize the damage to healthy tissue and to maximize the dose in the tumor. This is done according to an optimization method. One such method is the least squares difference between the dose actually deposited in the tumor and the desired dose. Forward transport can be used to calculate the sensitivity of the dose delivered to the patient, caused by small changes in energy or position of the source [3].

Figure 2 shows the irradiation from one source position (beam). The forward analysis establishes the response for every voxel in terms of dose deposited

per unit source weight [5]. A voxel is a small cube at a fixed position in a phantom and can represent (a part of) a tumor, a normal tissue, or an organ at risk (OAR). Particles emitted from a source position (beam) do not follow a straight line in a phantom because of scatter. Therefore, each source position has a different response. Combining the responses of all source positions in the best way using iterative selection gives the optimal beam selection.

Forward Transport

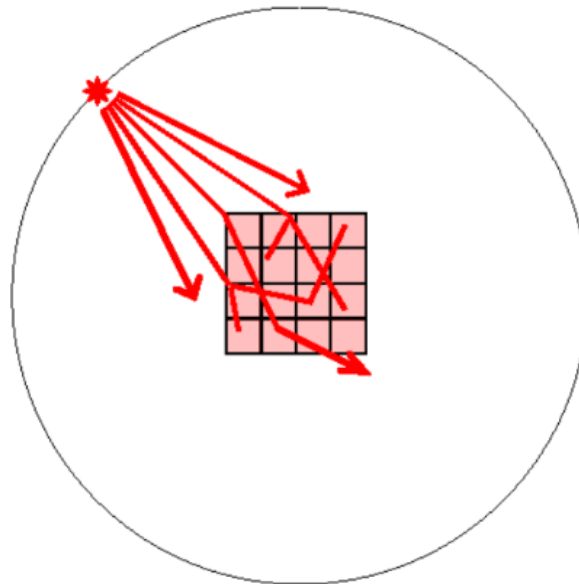


Figure 2: When forward transport is used, a predefined selection of beams and beam sources is made, and the optimal beam selection is improved after each iteration. The arrows indicate a route from a beam to the tumor voxels where the dose can be deposited [5].

Forward transport is more common than adjoint transport, but adjoint transport looks more promising for the future in terms of computation speed and accuracy. In this report, forward transport will be used to calculate the final dose deposition, which will serve as validation. The input parameters for forward transport will be determined by adjoint transport.

1.3.2 Adjoint transport

Adjoint transport considers a grid of voxels inside a phantom and predicts the response of the voxels relative to all possible source parameters (the beam positions) by reversing the radiation transport [5]. It can be thought of as particle transport in opposite direction. The particles emitted from a source position (voxel) do not follow a straight line because of 'inverse' scatter, where the protons start with an energy of $E = 0$ and *gain* energy along their path. Therefore, each source position, a tumor voxel, has a different response. During the adjoint calculation, importance functions are generated.

The importance functions provided by adjoint transport (also called adjoint functions) illustrate how important each beam position is for delivering dose to each voxel. Figure 3 considers the response for a single voxel. The adjoint analysis establishes the dose in that voxel as a function of all possible beam positions [5]. A selection of beams can be made after combining the results of all voxels, since all importance functions together illustrate which beams are the most important ones for all voxels. The optimal beams can also be determined by calculating the ratio of the intensity of the doses in the tumor and in the rest of the organs for each voxel to beam ray. The rays with the best ratios are selected and will be converted in beam positions and directions. This forms the optimal set of beams. However, an iterative algorithm can still be performed for minor improvements in beam weights [3].

Adjoint Transport

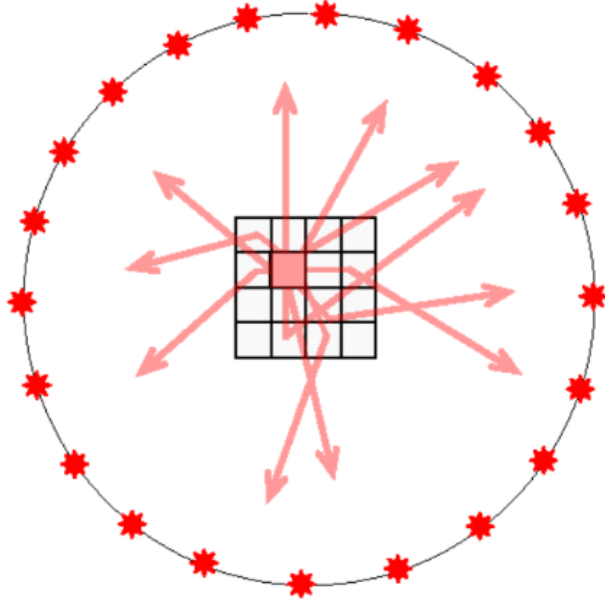


Figure 3: Importance distributions can be generated for each voxel using adjoint transport. The arrows indicate a route from a single tumor voxel to the possible source positions. Ultimately, the source positions selected by the arrows have to deliver the dose in the voxels [5].

The power of adjoint theory is that it can calculate (small) changes in response for each possible scenario from a reference state up to first order (for example movements of the patient) [21]. Once adjoint transport is done correctly, only one calculation run is needed to obtain all necessary results. After selecting the optimal beams and directions, the weight of each beam can be adjusted as well using iterative optimization.

1.4 Goal of this research

This research investigates how optimal beam angles and beam weights can be selected in a fast and efficient way to minimize tissue damage and maximise tumor damage. Therefore, the 'adjoint method' is developed based on previous work [15], [18], [20], [21]. These works investigated adjoint transport for a single beam in one direction [20], performed ray-tracing through a phantom [15], determined several uncertainties of adjoint transport [21],

and looked at various specific operators of the Linear Boltzmann Transport Equation [18], respectively.

The adjoint method is performed by expanding adjoint transport to three dimensions for multiple beams in multiple directions. This information is then updated using an iterative optimization algorithm and used as input for forward transport where the dose deposition will be calculated. The following research-question for the adjoint method is formulated:

How accurate is the adjoint method in choosing a selection of optimal beam angles and beam weights for radiotherapy treatment planning?

The adjoint method focuses on speed and is still useful, when small deviations occur during the process. The research-question is answered by investigating the following sub-questions:

- How does the adjoint method work?
- How is the adjoint method solved?

The results might give additional insights or defects that can be of importance in future work.

1.5 Thesis outline

In Chapter 2, proton transport is described. This chapter explains the Linear Boltzmann Transport Equation and the Fokker-Planck approximation, which both describe the behaviour of protons in a medium. Besides, all discretizations to solve the numerical computations are explained. Chapter 3 describes the adjoint theory, which is needed to find the optimal selection of beam angles and beam weights. Results of the adjoint method for a simple set-up are shown in Chapter 4. Finally, conclusions and recommendations are given in Chapter 5.

2 Proton transport

The behaviour of protons in a medium plays an important role in their dose distributions. Interactions such as scatter and absorption can change the direction and energy of protons. The Linear Boltzmann Transport Equation (LBTE) describes this behaviour and equates different gain and loss terms of protons. The LBTE is stated in Section 2.1, together with all its individual terms and assumptions. Approximations of the LBTE can be made, since only protons are used. This results in the Fokker-Planck approximation and is explained in Section 2.2. Discretizations of all terms of the Fokker-Planck approximation are made in Section 2.3 to solve the problem numerically. This includes the Discontinuous Galerkin (DG) method for the energy domain (Section 2.3.1) and the Crank-Nicolson (C-N) method for the spatial domain (Section 2.3.4). Finally, the dose calculation is explained in Section 2.4.

2.1 Linear Boltzmann Transport Equation

The Linear Boltzmann Transport Equation describes the behaviour of particles in a medium. Duderstadt and Hamilton [1] explain in detail the derivation of the LBTE in their work. Equation (2.1) defines the LBTE:

$$\hat{\Omega} \cdot \nabla \phi(\mathbf{r}, E, \hat{\Omega}) + \Sigma_t(\mathbf{r}, E) \phi(\mathbf{r}, E, \hat{\Omega}) = \int_{4\pi} \int_0^\infty \Sigma_s(\mathbf{r}, E' \rightarrow E, \hat{\Omega}' \rightarrow \hat{\Omega}) \phi(\mathbf{r}, E', \hat{\Omega}') dE' d\hat{\Omega}' + s(\mathbf{r}, E, \hat{\Omega}). \quad (2.1)$$

$\phi(\mathbf{r}, E, \hat{\Omega})$ is the angular particle flux, the main variable in Equation (2.1). The angular flux is a scalar quantity and depends on six parameters: three spatial, one energy and two angular. It represents the distribution of the number of particles passing through a unit surface located at \mathbf{r} , having energy E and moving in direction $\hat{\Omega}$. Interactions with the medium may cause changes in the angular flux and are represented by the terms in Equation (2.1) [1].

The streaming operator is the first term on the left hand side in Equation (2.1). It represents the net flow of particles. The total removal term is the next term, in which $\Sigma_t(\mathbf{r}, E)$ is the total macroscopic cross-section of the particles, denoting the probability of any interaction (scatter, absorption etc.) per unit distance travelled. The total removal term describes the loss of particles with energy E and direction $\hat{\Omega}$ due to collisions. For example, these particles may be absorbed or their energy and direction altered because of

scattering of another particle. The scatter operator is the first term on the right hand side, in which $\Sigma_s(\mathbf{r}, E)$ is the macroscopic scatter cross-section of the particles. It represents the probability that a particle changes from energy E' to E and from direction $\hat{\Omega}'$ to $\hat{\Omega}$ after scattering. It is therefore a gain term. The source term is the final term in Equation (2.1) and is a gain term as well. Only particles emitted in the medium with energy E and direction $\hat{\Omega}$ contribute to the balance equation.

Duderstadt and Hamilton [1] assumed the following statements when they derived the LBTE. These assumptions have to be justified for protons, which are used in this research.

- **The LBTE is in steady-state.** The proton flux reaches instantaneously steady-state after irradiation of the patient and is therefore justified. Besides, the medium will not change drastically during irradiation because of the small number of protons used compared to tissue atoms.
- **The LBTE describes the average behaviour of the particles.** Only the average deposited dose is required to calculate the total deposited dose by the protons. The knowledge of the dose deposition of each individual proton is not necessary.
- **The free motion of particles can be described using classical mechanics.** Quantum mechanical effects are not present in the clinical proton energy range.
- **There are no proton-proton interactions.** A proton-proton interaction is unlikely, since the particle density of protons is very small in comparison with the density of tissue-atoms (several orders of magnitude).
- **Three body collisions are negligible.** Again, the density of protons compared with the density of irradiated tissue is so small that three body collisions are negligible.

All assumptions made by Duderstadt and Hamilton are valid for this research. Therefore, the LBTE can be used in the next step to derive the Fokker-Planck approximation.

2.2 Fokker-Planck approximation

The Fokker-Planck (F-P) approximation is based on the Linear Boltzmann Transport Equation, but it uses two approximations. Firstly, protons are

positively charged and interact with Coulomb forces through the medium. They can scatter elastically and inelastically to lose energy. However, these energy losses are very small and therefore a Taylor approximation can be done around $\Delta E = 0$ [12]. Therefore, the elastic scatter operation is replaced by a continuous scatter operation. Secondly, the Fokker-Planck equation assumes a small scatter angle such that the energy transfer is only peaked straightforward [12]. The Fokker-Planck equation is given in Equation (2.2):

$$\hat{\Omega} \cdot \nabla \phi(\mathbf{r}, E, \hat{\Omega}) + \Sigma_a(\mathbf{r}, E) \phi(\mathbf{r}, E, \hat{\Omega}) = \frac{\Sigma_{tr}(\mathbf{r}, E)}{2} \nabla_{\hat{\Omega}}^2 \phi(\mathbf{r}, E, \hat{\Omega}) + \frac{\partial S(\mathbf{r}, E) \phi(\mathbf{r}, E, \hat{\Omega})}{\partial E} + \frac{1}{2} \frac{\partial^2 T(\mathbf{r}, E) \phi(\mathbf{r}, E, \hat{\Omega})}{\partial E^2} + s(\mathbf{r}, E, \hat{\Omega}). \quad (2.2)$$

The removal term from Equation (2.1) is replaced by an absorption and a scatter term. The absorption term, in which $\Sigma_a(\mathbf{r}, E)$ is the absorption cross-section, is the second term on the left hand side of Equation (2.2). The scatter term is combined with the scatter operator from Equation (2.1) and results in the first three terms on the right hand side. The diffusion term is the first term on the right hand side, in which $\Sigma_{tr}(\mathbf{r}, E)$ is the macroscopic transport cross-section. $\Sigma_{tr}(\mathbf{r}, E)$ states the probability a proton will diffuse per unit distance travelled. The continuous slowing down (CSD) operator is the second term on the right hand side. It is the first-order term of the Taylor expansion about $\Delta E = 0$ [21] and represents a continuous energy transfer from the protons to surrounding atoms. $S(\mathbf{r}, E)$ is the stopping power coefficient and describes how quickly protons slow down and lose their energy. The straggling operator is the third term, which is the second-order term of the Taylor expansion about $\Delta E = 0$ [21]. It represents the stochastic behaviour of the interaction process between a proton and its surrounding medium. $T(\mathbf{r}, E)$ is the energy straggling coefficient and expresses the statistical variation around the mean of the energy loss of a proton. Specific expressions for $S(\mathbf{r}, E)$ and $T(\mathbf{r}, E)$ can be found in Burlacu's work [18].

This study focuses on the slowing down operator and the straggling operator only. Therefore, absorption, diffusion, and elastic scatter are not considered. The F-P approximation becomes the following:

$$\hat{\Omega} \cdot \nabla \phi(\mathbf{r}, E) = \frac{\partial S(\mathbf{r}, E) \phi(\mathbf{r}, E)}{\partial E} + \frac{1}{2} \frac{\partial^2 T(\mathbf{r}, E) \phi(\mathbf{r}, E)}{\partial E^2} + s(\mathbf{r}, E). \quad (2.3)$$

This can be written more conveniently as:

$$\hat{\Omega} \cdot \nabla \phi(\mathbf{r}, E) = \frac{\partial S^*(\mathbf{r}, E)\phi(\mathbf{r}, E)}{\partial E} + \frac{\partial}{\partial E} \left[T^*(\mathbf{r}, E) \frac{\partial \phi(\mathbf{r}, E)}{\partial E} \right] + s(\mathbf{r}, E), \quad (2.4)$$

where

$$\begin{aligned} S^*(\mathbf{r}, E) &= S(\mathbf{r}, E) + \frac{1}{2} \frac{\partial T(\mathbf{r}, E)}{\partial E}, \\ T^*(\mathbf{r}, E) &= \frac{1}{2} T(\mathbf{r}, E). \end{aligned} \quad (2.5)$$

The forward transport equation with $\mathbf{r} \in [0, L_x] \times [0, L_y] \times [0, L_z]$ and $E \in [E_{min}, E_{max}]$ is represented in Equation (2.3). The equation can be written as linear problem in a compact and discretized form:

$$L\phi = s. \quad (2.6)$$

L represents all Fokker-Planck operators and s the source. The corresponding initial and boundary conditions are given in Equation (2.7):

$$\begin{aligned} \phi(\mathbf{r}, E) &= \phi_0(E), \quad \hat{\Omega} \cdot \hat{\mathbf{n}} < 0, \quad \mathbf{r} \in \partial V, \\ \frac{\partial \phi(\mathbf{r}, E_{min})}{\partial E} &= 0, \\ \phi(\mathbf{r}, E_{max}) &= 0. \end{aligned} \quad (2.7)$$

The first condition shows that ϕ only has a non-zero value at the boundary, $\mathbf{r} \in \partial V$, if the beam is pointing towards the phantom. $\hat{\Omega}$ is the direction of the transport and $\hat{\mathbf{n}}$ is the outward pointing normal unit on the boundary. The first boundary condition prevents the particles from reaching a negative energy value, since the lowest energy group E_{min} has a derivative of zero. The particles cannot lose any energy when arriving at the lowest possible energy value and therefore they cannot contribute to the dose anymore. The second boundary condition describes the upper limit in E . Zero particles are present within energy group $E = E_{max}$. It prevents particles having an infinite amount of energy.

2.3 Discretization

This section describes all necessary discretizations to solve the Fokker-Planck approximation numerically. The Discontinuous Galerkin (DG) method is used to discretize the energy domain and is explained in Section 2.3.1. The Crank-Nicolson (C-N) method is used to perform ray-tracing in the spatial domain, see Section 2.3.4. Besides, the operators of the Fokker-Planck approximation are discretized in Sections 2.3.2 and 2.3.3. The linear system is transformed into a set of algebraic equations. This is then solved using the DGBSV routine from the LAPACK package [4]. Finally, a small note about boundary discretization is given in Section 2.3.5.

2.3.1 Energy domain - Discontinuous Galerkin

The energy in the transport equation is discretized using the multi-group method. The energy domain is divided into NG equally sized cells, where NG is the number of groups. A specific energy group is denoted by E_g . The highest energy group, E_{NG} , has the lowest energy, while the lowest energy group, E_1 , has the highest energy. The boundaries of energy group E_g are represented by $E_{g\pm\frac{1}{2}}$, see Figure 4. In this thesis, no inflow of flux is present in the lowest energy group, E_1 . Since protons lose their energy, they flow from the lowest group E_1 to higher energy groups E_g . Protons that arrive in energy group E_{NG} have lost all their energy.

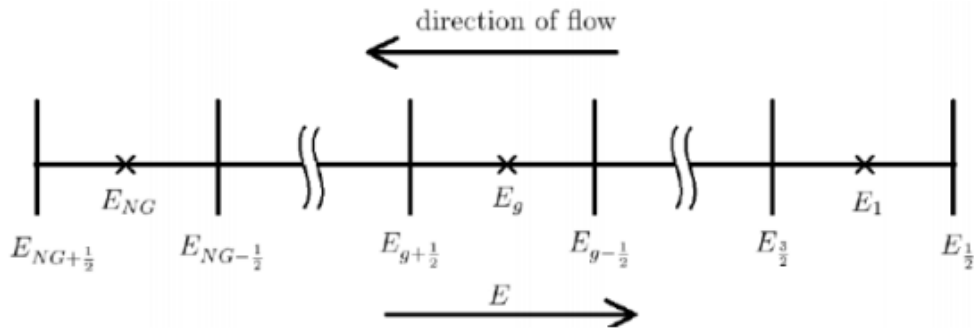


Figure 4: Representation of the multi-group method. The energy is flowing from a low energy group to a high energy group, while the absolute energy is going in opposite direction. NG is the total number of groups [12].

In the Disontinuous Galerkin (DG) method, two values are present at the boundary of an energy group. This results in discontinuities at the boundary,

see Figure 5. The flux distribution of group g can be described by using a first-order polynomial on the flux. This is done in Equation (2.8):

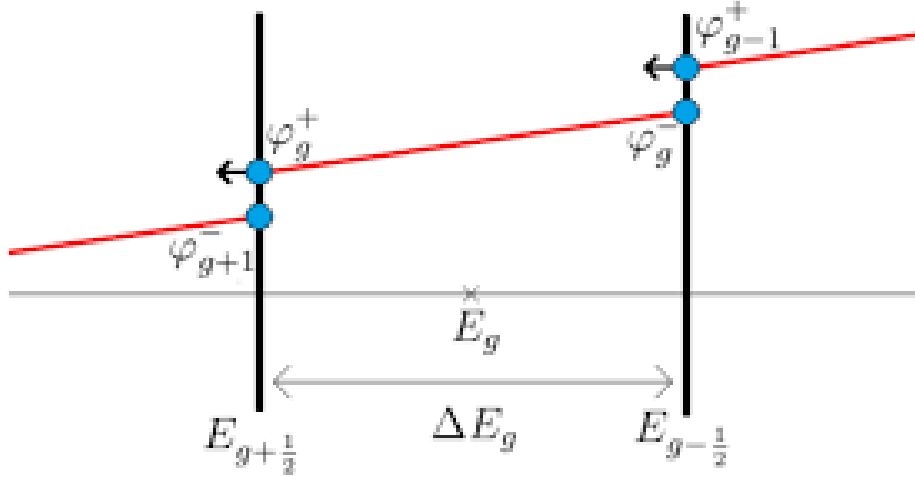


Figure 5: Representation of the DG-method. An energy group has a size ΔE_g . At the boundaries, a discrete step can be taken to arrive in the next or previous group [12].

$$\phi(\mathbf{r}, E) = \phi_g^0(\mathbf{r})h_g^0(E) + \phi_g^1(\mathbf{r})h_g^1(E). \quad (2.8)$$

$h_g^i(E)$ denotes basis function i and ϕ_g^i are the expansion coefficients. Two basis functions represent the average (A) and the slope (E) of group g . Since only a first-order polynomial is taken, this is enough to form the complete flux of an energy group. Equation (2.9) represents the chosen basis functions:

$$\begin{aligned} h^A(E) &= h^0(E) = 1, \\ h^E(E) &= h^1(E) = \frac{2}{\Delta E_g}(E - E_g). \end{aligned} \quad (2.9)$$

The basis functions are orthogonal. Therefore, Equation (2.10) holds:

$$\int_{E_{g+1/2}}^{E_{g-1/2}} h^i(E)h^j(E)dE = \frac{\Delta E_g}{2j+1}\delta_{ij}. \quad (2.10)$$

This approach results in two coefficients for each energy group, the average flux ϕ^0 and the normalized slope of the flux ϕ^1 . The flux ϕ is a result of both coefficients (Equation (2.8)). Two equations per group are needed to actually solve the system, since two coefficients per group are present. This is done by numerical solving using the Crank-Nicolson method (Section 2.3.4).

2.3.2 Continuous Slowing Down operator

First, the energy dependence of the continuous slowing down (CSD) operator is discretized. The contribution of the CSD operator on the flux is given in Equation (2.11):

$$L_{CSD}(\cdot) = \frac{\partial S^*(\mathbf{r}, E)}{\partial E}(\cdot). \quad (2.11)$$

Two algebraic equations are necessary to solve the average and normalized slope of the angular flux. They are obtained by multiplying Equation (2.11) with the two basis functions defined in Equation (2.9). Then, the equation is integrated over the domain. First, Equation (2.11) is multiplied with the first basis function and integrated over an energy group:

$$\int_{E_{g+\frac{1}{2}}}^{E_{g-\frac{1}{2}}} \frac{\partial}{\partial E} (S^*(\mathbf{r}, E)\phi(\mathbf{r}, E)) h^0(E) dE = \\ [S^*(\mathbf{r}, E)\phi(\mathbf{r}, E)h^0(E)]_{E_{g+\frac{1}{2}}}^{E_{g-\frac{1}{2}}} - \int_{E_{g+\frac{1}{2}}}^{E_{g-\frac{1}{2}}} S^*(\mathbf{r}, E)\phi(\mathbf{r}, E) \frac{\partial h^0(E)}{\partial E} dE. \quad (2.12)$$

The integral term on the right side equals zero. Equation (2.13) is obtained, when evaluating the term with the brackets. The result is an expression for the CSD operator when multiplied with the first basis function.

$$\begin{aligned}
\int_{E_{g+\frac{1}{2}}}^{E_{g-\frac{1}{2}}} \frac{\partial}{\partial E} (S^*(\mathbf{r}, E)\phi(\mathbf{r}, E)) h^0(E) dE = \\
S^*(\mathbf{r}, E_{g-\frac{1}{2}})\phi(\mathbf{r}, E_{g-\frac{1}{2}}) - S^*(\mathbf{r}, E_{g+\frac{1}{2}})\phi(\mathbf{r}, E_{g+\frac{1}{2}}) = \\
S^*(\mathbf{r}, E_{g-\frac{1}{2}}) \left(\phi_{g-1}^0(\mathbf{r})h_{g-1}^0(E) + \phi_{g-1}^1(\mathbf{r})h_{g-1}^1(E_{g-\frac{1}{2}}) \right) - \\
S^*(\mathbf{r}, E_{g+\frac{1}{2}}) \left(\phi_g^0(\mathbf{r})h_g^0(E) + \phi_g^1(\mathbf{r})h_g^1(E_{g+\frac{1}{2}}) \right) = \\
S^*(\mathbf{r}, E_{g-\frac{1}{2}}) \left(\phi_{g-1}^0(\mathbf{r}) + \phi_{g-1}^1(\mathbf{r}) \right) - S^*(\mathbf{r}, E_{g+\frac{1}{2}}) \left(\phi_g^0(\mathbf{r}) - \phi_g^1(\mathbf{r}) \right). \quad (2.13)
\end{aligned}$$

Equation (2.14) is obtained when multiplying Equation (2.11) with the second basisfunction and integrating over an energy group:

$$\begin{aligned}
\int_{E_{g+\frac{1}{2}}}^{E_{g-\frac{1}{2}}} \frac{\partial}{\partial E} (S^*(\mathbf{r}, E)\phi(\mathbf{r}, E)) h^1(E) dE = \\
[S^*(\mathbf{r}, E)\phi(\mathbf{r}, E)h^1(E)]_{E_{g+\frac{1}{2}}}^{E_{g-\frac{1}{2}}} - \int_{E_{g+\frac{1}{2}}}^{E_{g-\frac{1}{2}}} S^*(\mathbf{r}, E)\phi(\mathbf{r}, E) \frac{\partial h^1(E)}{\partial E} dE. \quad (2.14)
\end{aligned}$$

Evaluating the brackets results in:

$$\begin{aligned}
[S^*(\mathbf{r}, E)\phi(\mathbf{r}, E)h^1(E)]_{E_{g+\frac{1}{2}}}^{E_{g-\frac{1}{2}}} = \\
S^*(\mathbf{r}, E_{g-\frac{1}{2}}) \left(\phi_{g-1}^0(\mathbf{r}) - \phi_{g-1}^1(\mathbf{r}) \right) + S^*(\mathbf{r}, E_{g+\frac{1}{2}}) \left(\phi_g^0(\mathbf{r}) - \phi_g^1(\mathbf{r}) \right). \quad (2.15)
\end{aligned}$$

The last term in Equation (2.14) is now non-zero. This integral can be evaluated using the orthogonal property stated in Equation (2.10). However, the stopping power has to be expanded in terms of the basis functions first:

$$\begin{aligned}
S^*(\mathbf{r}, E) = \frac{S^*(\mathbf{r}, E_{g-\frac{1}{2}}) + S^*(\mathbf{r}, E_{g+\frac{1}{2}})}{2} h^0(E) + \frac{S^*(\mathbf{r}, E_{g-\frac{1}{2}}) - S^*(\mathbf{r}, E_{g+\frac{1}{2}})}{2} h^1(E) = \\
S^{*0}(\mathbf{r}, E)h^0(E) + S^{*1}(\mathbf{r}, E)h^1(E). \quad (2.16)
\end{aligned}$$

Now, the integral can be rewritten and an expression for the last integral term in Equation (2.14) is obtained:

$$\begin{aligned} & \frac{2}{\Delta E_g} \int_{E_{g+\frac{1}{2}}}^{E_{g-\frac{1}{2}}} S^*(\mathbf{r}, E) \phi(\mathbf{r}, E) dE = \\ & \frac{2}{\Delta E_g} \int_{E_{g+\frac{1}{2}}}^{E_{g-\frac{1}{2}}} \left(S_g^{*0}(\mathbf{r}, E) h_g^0(E) + S_g^{*1}(\mathbf{r}, E) h_g^1(E) \right) \left(\phi_g^0(\mathbf{r}) h_g^0(E) + \phi_g^1(\mathbf{r}) h_g^1(E) \right) dE = \\ & \frac{2}{\Delta E_g} \left(S_g^{*0}(\mathbf{r}, E) h_g^0(E) \Delta E_g + S_g^{*1}(\mathbf{r}, E) h_g^1(E) \frac{\Delta E_g}{3} \right). \quad (2.17) \end{aligned}$$

Equation (2.18) gives the total result for the slope part of the CSD operator:

$$\begin{aligned} & \int_{E_{g+\frac{1}{2}}}^{E_{g-\frac{1}{2}}} \frac{\partial}{\partial E} (S^*(\mathbf{r}, E) \phi(\mathbf{r}, E)) h^1(E) dE = \\ & S^*(\mathbf{r}, E_{g-\frac{1}{2}}) \left(\phi_{g-1}^0(\mathbf{r}) - \phi_{g-1}^1(\mathbf{r}) \right) + S^*(\mathbf{r}, E_{g+\frac{1}{2}}) \left(\phi_g^0(\mathbf{r}) - \phi_g^1(\mathbf{r}) \right) - \\ & \frac{2}{\Delta E_g} \left(S_g^{*0}(\mathbf{r}, E) h_g^0(E) \Delta E_g + S_g^{*1}(\mathbf{r}, E) h_g^1(E) \frac{\Delta E_g}{3} \right). \quad (2.18) \end{aligned}$$

Equations (2.13) and (2.18) can be used to numerically solve the Fokker-Planck approximation using the Crank-Nicolson method.

2.3.3 Straggling operator

The Symmetric Interior Penalty Galerkin (SIPG) is a variant of the DG method. It is used to discretize the straggling operator. Equation (2.19) represents the energy straggling operator:

$$L_{ES}(\cdot) = \frac{\partial}{\partial E} T^*(\mathbf{r}, E) \frac{\partial(\cdot)}{\partial E}, \quad (2.19)$$

where $T^*(\mathbf{r}, E) = \frac{1}{2}T(\mathbf{r}, E)$. A variational formulation is used to obtain the SIPG specific bilinear form [9], [11]. Then, a system of ordinary linear differential equations can be made. This system solves the two unknowns ϕ^0 and ϕ^1 for every energy group. It is solved using the DGBSV routine from the linear Algebra package (LAPACK). The full derivation of the energy straggling operator and its discretizations can be found in the work of Burlacu [18].

2.3.4 Spatial domain - Crank-Nicolson

A set of linear equations, given in Equation (2.20), is obtained after discretizing the energy domain:

$$\frac{d\phi(\mathbf{r})}{dz} = L(\mathbf{r})\phi(\mathbf{r}). \quad (2.20)$$

$\phi(\mathbf{r})$ is written as a combination of the average and slope for each energy group, $\phi(\mathbf{r}) = [\phi_1^0(\mathbf{r}), \phi_1^1(\mathbf{r}) \dots \phi_g^0(\mathbf{r}), \phi_g^1(\mathbf{r}) \dots \phi_{NG}^0(\mathbf{r}), \phi_{NG}^1(\mathbf{r})]^T$, with NG the number of groups. $L(\mathbf{r})$ contains all variables of the operators in the Fokker-Planck approximation in a matrix. $\phi(\mathbf{r})$ is independent of E from now on. The Crank-Nicolson (C-N) method is used to solve this linear set of equations. This method uses three steps. First, the domain has to be discretized and fulfilled at discrete points. Then, finite difference approximations replace the derivatives. Finally, a recursive algorithm is formulated [13].

The spatial domain of the phantom is divided into NE uniform smaller cells. These cells are called voxels. Voxels are little cubes of size $\Delta x, \Delta y, \Delta z$. Voxels represent (a part of) a tumor, a normal tissue, or an organ at risk. Parameters such as the tissue type and the stopping power are bounded to each voxel. Smaller spatial steps can be taken within a voxel for more accurate computations, but within a voxel, all parameters are the same. The volume of a voxel has to be taken into account when calculating the adjoint source or dose deposition in a voxel.

The finite difference method calculates the solution only at discrete points and not at points in between. Using the C-N method, a central difference between grid points is constructed according to Equation (2.21):

$$z_{i+\frac{1}{2}} = \frac{(\mathbf{r}_i + \mathbf{r}_{i+1})}{2}. \quad (2.21)$$

When tracing a specific ray, all spatial grid points lay on one line. Therefore, this problem can be viewed as a 1D problem, where \mathbf{r}_i and \mathbf{r}_{i+1} can be seen as x_i and x_{i+1} , respectively. However, in the following equations, \mathbf{r} will still be used instead of x for convenience.

The finite difference approximation is given in Equation (2.22):

$$\left. \frac{d\phi(\mathbf{r})}{dz} \right|_{z_{i+\frac{1}{2}}} \approx \frac{\phi(\mathbf{r}_{i+1}) - \phi(\mathbf{r}_i)}{z_{i+1} - z_i}. \quad (2.22)$$

Equation (2.23) is obtained after applying the first two steps of the C-N method:

$$\left. \frac{d\phi(\mathbf{r})}{dz} \right|_{z_{i+\frac{1}{2}}} \approx \frac{\phi(\mathbf{r}_{i+1}) - \phi(\mathbf{r}_i)}{z_{i+1} - z_i} = L(\mathbf{r})\phi(\mathbf{r})|_{z_{i+\frac{1}{2}}}. \quad (2.23)$$

$L(z_{i+\frac{1}{2}})\phi(z_{i+\frac{1}{2}})$ is approximated as a mean of the neighboring points \mathbf{r}_i and \mathbf{r}_{i+1} to be able to make a recursion relation between $\phi(\mathbf{r}_i)$ and $\phi(\mathbf{r}_{i+1})$:

$$L(z_{i+\frac{1}{2}})\phi(z_{i+\frac{1}{2}}) \approx \frac{1}{2} (L(\mathbf{r}_i)\phi(\mathbf{r}_i) + L(\mathbf{r}_{i+1})\phi(\mathbf{r}_{i+1})). \quad (2.24)$$

This leads to:

$$\frac{\phi(\mathbf{r}_{i+1}) - \phi(\mathbf{r}_i)}{z_{i+1} - z_i} = \frac{1}{2} (L(\mathbf{r}_i)\phi(\mathbf{r}_i) + L(\mathbf{r}_{i+1})\phi(\mathbf{r}_{i+1})). \quad (2.25)$$

$L(\mathbf{r})$ is assumed to be constant within a cell. Therefore, Equation (2.25) can now be written as:

$$\frac{\phi(\mathbf{r}_{i+1}) - \phi(\mathbf{r}_i)}{z_{i+1} - z_i} = \frac{1}{2} L(z_{i+\frac{1}{2}}) \cdot (\phi(\mathbf{r}_i) + \phi(\mathbf{r}_{i+1})). \quad (2.26)$$

The recursive form is as follows:

$$\phi(\mathbf{r}_{i+1}) = \frac{1 + \frac{1}{2}L(z_{i+\frac{1}{2}})(z_{i+1} - z_i)}{1 - \frac{1}{2}L(z_{i+\frac{1}{2}})(z_{i+1} - z_i)} \phi(\mathbf{r}_i). \quad (2.27)$$

$\phi(\mathbf{r}_i)$ is already known, because of the initial boundary conditions. Therefore, $\phi(\mathbf{r}_{i+1})$ can be calculated using Equation (2.27).

2.3.5 Boundary conditions

The initial flux ϕ_0 is discretized the same way as the flux ϕ . An average and a slope coefficient is present for each energy group for every beam. The input of the forward problem (ϕ_0) is based on the results of the adjoint calculation. Since the forward problem and the adjoint problem are using the same discretization methods (Sections 2.3 and 3.5), no additional discretization of boundary conditions is needed.

2.4 Dose calculation and discretization

The deposited dose distribution in a phantom is one of the main interests in this thesis. The deposited dose is calculated by multiplying the Fokker-Planck approximation (Equation (2.3)) by the energy E and then integrating over the domain. This is done in Equation (2.28):

$$\int_{E_{min}}^{E_{max}} \hat{\Omega} \cdot \nabla \phi(\mathbf{r}, E) E dE = \int_{E_{min}}^{E_{max}} \left(\frac{\partial S^*(\mathbf{r}, E) \phi(\mathbf{r}, E)}{\partial E} + \frac{\partial}{\partial E} \left[T^*(\mathbf{r}, E) \frac{\partial \phi(\mathbf{r}, E)}{\partial E} \right] \right) E dE. \quad (2.28)$$

The continuous slowing down term and the straggling term will now be handled separately to calculate the dose deposition. The CSD operator is integrated by parts in Equation (2.29):

$$\int_{E_{min}}^{E_{max}} \left(\frac{\partial S^*(\mathbf{r}, E) \phi(\mathbf{r}, E)}{\partial E} \right) E dE = [S^*(\mathbf{r}, E) \phi(\mathbf{r}, E) E]_{E_{min}}^{E_{max}} - \int_{E_{min}}^{E_{max}} \frac{\partial S^*(\mathbf{r}, E) \phi(\mathbf{r}, E)}{\partial E} dE. \quad (2.29)$$

The boundary condition $\phi(\mathbf{r}, E_{max}) = 0$ is applied to obtain a dose expression for the CSD term:

$$\int_{E_{min}}^{E_{max}} \left(\frac{\partial S^*(\mathbf{r}, E) \phi(\mathbf{r}, E)}{\partial E} \right) E dE = - S^*(\mathbf{r}, E_{min}) \phi(\mathbf{r}, E_{min}) E_{min} - \int_{E_{min}}^{E_{max}} \frac{\partial S^*(\mathbf{r}, E) \phi(\mathbf{r}, E)}{\partial E} dE. \quad (2.30)$$

The same steps are done for the straggling term, starting with integration by parts:

$$\int_{E_{min}}^{E_{max}} \left(\frac{\partial}{\partial E} \left[T^*(\mathbf{r}, E) \frac{\partial \phi(\mathbf{r}, E)}{\partial E} \right] \right) E dE = \left[T^*(\mathbf{r}, E) \frac{\partial \phi(\mathbf{r}, E)}{\partial E} E \right]_{E_{min}}^{E_{max}} - \int_{E_{min}}^{E_{max}} T^*(\mathbf{r}, E) \frac{\partial \phi(\mathbf{r}, E)}{\partial E} dE. \quad (2.31)$$

Applying the boundary conditions $\phi(\mathbf{r}, E_{max}) = 0$ and $\frac{\partial \phi(\mathbf{r}, E_{min})}{\partial E} = 0$ results in:

$$\int_{E_{min}}^{E_{max}} \left(\frac{\partial}{\partial E} \left[T^*(\mathbf{r}, E) \frac{\partial \phi(\mathbf{r}, E)}{\partial E} \right] \right) E dE = - \int_{E_{min}}^{E_{max}} T^*(\mathbf{r}, E) \frac{\partial \phi(\mathbf{r}, E)}{\partial E} dE. \quad (2.32)$$

The total loss of energy at point \mathbf{r} is now obtained:

$$\int_{E_{min}}^{E_{max}} \hat{\Omega} \cdot \nabla \phi(\mathbf{r}, E) E dE = -S^*(\mathbf{r}, E_{min}) \phi(\mathbf{r}, E_{min}) E_{min} - \int_{E_{min}}^{E_{max}} \frac{\partial S^*(\mathbf{r}, E) \phi(\mathbf{r}, E)}{\partial E} dE - \int_{E_{min}}^{E_{max}} T^*(\mathbf{r}, E) \frac{\partial \phi(\mathbf{r}, E)}{\partial E} dE. \quad (2.33)$$

Since the gain in energy is the opposite of the loss in energy, the dose can be written as is done in Equation (2.34):

$$D(\mathbf{r}) = S^*(\mathbf{r}, E_{min}) \phi(\mathbf{r}, E_{min}) E_{min} + \int_{E_{min}}^{E_{max}} \frac{\partial S^*(\mathbf{r}, E) \phi(\mathbf{r}, E)}{\partial E} dE + \int_{E_{min}}^{E_{max}} T^*(\mathbf{r}, E) \frac{\partial \phi(\mathbf{r}, E)}{\partial E} dE. \quad (2.34)$$

The integrated dose is then given by R :

$$R = \int_{\mathbf{r}_{min}}^{\mathbf{r}_{max}} D(\mathbf{r}) d\mathbf{r}. \quad (2.35)$$

This integrated dose can be calculated for all kinds of regions of interest, such as a single beam, a single voxel or a group of voxels. In this thesis, the integrated dose of interest is over single voxels.

The dose needs to be discretized in terms of the average and the slope of the flux, $\phi_g^0(\mathbf{r})$ and $\phi_g^1(\mathbf{r})$ respectively, since this is also done for the Fokker-Planck approximation (Equation (2.3)). Equation (2.36) shows the result of discretizing Equation (2.34) using the same steps as in Section 2.3:

$$\begin{aligned}
D(\mathbf{r}) = & E_{min}S(E_{min}) [\phi_{NG}^0(\mathbf{r}) - \phi_{NG}^1(\mathbf{r})] + \\
& \sum_{g=1}^{NG} \int_{E_{g+\frac{1}{2}}}^{E_{g-\frac{1}{2}}} [\phi_g^0(\mathbf{r})h^0(E) + \phi_g^1(\mathbf{r})h^1(E)] [S^{*0}(\mathbf{r}, E)h^0(E) + S^{*1}(\mathbf{r}, E)h^1(E)] dE + \\
& \sum_{g=1}^{NG} \int_{E_{g+\frac{1}{2}}}^{E_{g-\frac{1}{2}}} (T^{*0}(\mathbf{r}, E)h^0(E) + T^{*1}(\mathbf{r}, E)h^1(E)) \frac{2}{\Delta E_g} \phi_g^1(\mathbf{r}) dE. \quad (2.36)
\end{aligned}$$

In Equation (2.36), the straggling term is expanded in terms of its basis functions. Performing the integral and using the orthogonality property for both terms results in:

$$\begin{aligned}
D(\mathbf{r}) = & E_{min}S(E_{min}) [\phi_{NG}^0(\mathbf{r}) - \phi_{NG}^1(\mathbf{r})] + \\
& \sum_{g=1}^{NG} \left[\phi_g^0(\mathbf{r})S^{*0}(\mathbf{r}, E)\Delta E_g + \phi_g^1(\mathbf{r})S^{*1}(\mathbf{r}, E)\frac{\Delta E_g}{3} \right] + \\
& \sum_{g=1}^{NG} \frac{2}{\Delta E_g} \phi_g^1(\mathbf{r}) \left(T^{*0}(\mathbf{r}, E)\Delta E_g + \frac{T^{*1}(\mathbf{r}, E)}{\Delta E_g} (E_{g-\frac{1}{2}}^2 - E_{g+\frac{1}{2}}^2) - 2T^{*1}(\mathbf{r}, E)\Delta E_g \right). \quad (2.37)
\end{aligned}$$

The integral dose can then be calculated over the domain $\mathbf{r} \in [\mathbf{r}_{min}, \mathbf{r}_{max}]$. After normalizing the dose to the average dose over a certain region, it can be used as input for the adjoint source for iteration.

3 Adjoint method

This chapter explains the adjoint theory. The adjoint theory is necessary to predict the response of a source. If small perturbations are applied to the problem, the new solution can be approximated quickly, because of the linear character of adjoint transport. In Section 3.1, the adjoint Fokker-Planck approximation is derived. Then, a perturbation analysis is done in Section 3.2. The adjoint source is formulated in Section 3.3. The gradient descent method is used to update the boundary conditions in order to obtain a better objective value as fast as possible. This is described in Section 3.4. Discretizations for the adjoint terms are made in Section 3.5 and finally, the beam angle selection method is briefly explained in Section 3.6.

3.1 Adjoint Fokker-Planck approximation

An adjoint operator A^\dagger is defined according to Equation (3.1) [1]:

$$\langle A\phi, \phi^\dagger \rangle = \langle \phi, A^\dagger\phi^\dagger \rangle + \text{Boundary terms.} \quad (3.1)$$

$\langle (\cdot), (\cdot) \rangle$ represents an inner product. A is an operator working on ϕ , the flux. A^\dagger and ϕ^\dagger are then called the adjoint operator and the adjoint flux, respectively. The boundary conditions should be chosen such that the boundary terms are equal to zero.

The linear forward problem in Equation (2.6) has an adjoint counterpart:

$$L^\dagger\phi^\dagger = s^\dagger. \quad (3.2)$$

L^\dagger represents all adjoint operators and s^\dagger is the adjoint source. An important property of the adjoint is additivity, see Equation (3.3):

$$(A_1 + A_2 + \dots)^\dagger = A_1^\dagger + A_2^\dagger + \dots \quad (3.3)$$

The adjoint transport equation can be formulated when all terms of the forward Fokker-Planck (2.3) approximation are transformed to their adjoint. Following the definition of an adjoint operator stated in Equation (3.1), the adjoint version of the continuous slowing down operator can be derived. In Equation (3.4) the first step of the derivation is done:

$$\langle L_{CSD}\phi, \phi^\dagger \rangle = \int_0^{\mathbf{r}} \int_0^\infty \frac{\partial S^*(\mathbf{r}, E)\phi(\mathbf{r}, E)}{\partial E} \phi^\dagger(\mathbf{r}, E) dE d\mathbf{r}. \quad (3.4)$$

Equation (3.5) shows the result after integration by parts on the right hand side:

$$\int_0^{\mathbf{r}} [S^*(\mathbf{r}, E)\phi(\mathbf{r}, E)\phi^\dagger(\mathbf{r}, E)]_{E=0}^{E=\infty} d\mathbf{r} - \int_0^{\mathbf{r}} \int_0^\infty S^*(\mathbf{r}, E)\phi(\mathbf{r}, E) \frac{\partial \phi^\dagger(\mathbf{r}, E)}{\partial E} dE d\mathbf{r}. \quad (3.5)$$

The boundary terms for the adjoint are still unknown, but if they are chosen right, the first term will become zero. Therefore, the boundary conditions for the adjoint is $\phi^\dagger(\mathbf{r}, E_{min}) = 0$, since the known boundary condition of the forward flux is $\phi(\mathbf{r}, E_{max}) = 0$ (Equation (2.7)). The result is:

$$\langle \phi, L_{CSD}^\dagger \phi^\dagger \rangle = - \int_0^{\mathbf{r}} \int_0^\infty S^*(\mathbf{r}, E)\phi(\mathbf{r}, E) \frac{\partial \phi^\dagger(\mathbf{r}, E)}{\partial E} dE d\mathbf{r}. \quad (3.6)$$

Therefore, the adjoint continuous slowing down operator is the following:

$$L_{CSD}^\dagger(\cdot) = -S^*(\mathbf{r}, E) \frac{\partial}{\partial E}(\cdot). \quad (3.7)$$

Similar steps can be taken for the energy straggling operator. First, the inner product is applied in Equation (3.8):

$$\langle L_{ES}\phi, \phi^\dagger \rangle = \int_0^{\mathbf{r}} \int_0^\infty \frac{\partial}{\partial E} \left[T^*(\mathbf{r}, E) \frac{\partial \phi(\mathbf{r}, E)}{\partial E} \right] \phi^\dagger(\mathbf{r}, E) dE d\mathbf{r}. \quad (3.8)$$

Equation (3.9) shows the result after integration by parts on the right hand side:

$$\int_0^{\mathbf{r}} \left[T^*(\mathbf{r}, E) \frac{\partial \phi(\mathbf{r}, E)}{\partial E} \phi^\dagger(\mathbf{r}, E) \right]_{E=0}^{E=\infty} d\mathbf{r} - \int_0^{\mathbf{r}} \int_0^\infty T^*(\mathbf{r}, E) \frac{\partial \phi(\mathbf{r}, E)}{\partial E} \frac{\partial \phi^\dagger(\mathbf{r}, E)}{\partial E} dE d\mathbf{r}. \quad (3.9)$$

Again, the boundary term should vanish if the boundary condition is chosen right. Therefore, the boundary conditions for the adjoint is $\frac{\partial \phi^\dagger(\mathbf{r}, E_{max})}{\partial E} = 0$, because in the forward problem, the boundary condition $\frac{\partial \phi(\mathbf{r}, E_{min})}{\partial E} = 0$ was already used. The remaining term is again integrated by parts:

$$- \int_0^{\mathbf{r}} \left[T^*(\mathbf{r}, E) \phi(\mathbf{r}, E) \frac{\partial \phi^\dagger(\mathbf{r}, E)}{\partial E} \right]_{E=0}^{E=\infty} d\mathbf{r} + \int_0^{\mathbf{r}} \int_0^\infty \frac{\partial}{\partial E} \left[T^*(\mathbf{r}, E) \frac{\partial \phi^\dagger(\mathbf{r}, E)}{\partial E} \right] \phi(\mathbf{r}, E) dE d\mathbf{r}. \quad (3.10)$$

The boundary term again vanishes, since $\frac{\partial \phi^\dagger(\mathbf{r}, E_{max})}{\partial E} = 0$ and $\phi^\dagger(\mathbf{r}, E_{min}) = 0$. The result is Equation (3.11):

$$\langle \phi, L_{SE}^\dagger \phi^\dagger \rangle = \int_0^{\mathbf{r}} \int_0^\infty \frac{\partial}{\partial E} \left[T^*(\mathbf{r}, E) \frac{\partial \phi^\dagger(\mathbf{r}, E)}{\partial E} \right] \phi(\mathbf{r}, E) dE d\mathbf{r}. \quad (3.11)$$

Therefore, the adjoint straggling operator is the following:

$$L_{SE}^\dagger(\cdot) = \frac{\partial}{\partial E} T^*(\mathbf{r}, E) \frac{\partial}{\partial E}(\cdot) = L_{SE}(\cdot). \quad (3.12)$$

The adjoint Fokker-Planck approximation is given in Equation (3.13), using the results of the adjoint operators:

$$-\hat{\Omega} \cdot \nabla \phi^\dagger(\mathbf{r}, E) = -S^*(\mathbf{r}, E) \frac{\partial \phi^\dagger(\mathbf{r}, E)}{\partial E} + \frac{\partial}{\partial E} \left[T^*(\mathbf{r}, E) \frac{\partial \phi^\dagger(\mathbf{r}, E)}{\partial E} \right] + s^\dagger(\mathbf{r}, E). \quad (3.13)$$

The corresponding boundary conditions are given in Equation (3.14):

$$\begin{aligned} \phi^\dagger(\mathbf{r}, E) &= 0, \quad \hat{\Omega} \cdot \hat{\mathbf{n}} > 0, \quad \mathbf{r} \in \partial V, \\ \frac{\partial \phi^\dagger(\mathbf{r}, E_{max})}{\partial E} &= 0, \\ \phi^\dagger(\mathbf{r}, E_{min}) &= 0. \end{aligned} \quad (3.14)$$

Compared to the forward Fokker-Planck equation (Equation (2.2)), only the signs of the streaming operator and the continuous slowing down operator have changed. A negative streaming operator implies that the protons stream in the opposite direction as in the forward transport equation. A negative continuous slowing down operator tells that the particles are gaining energy instead of losing it. The boundary conditions are in fact the opposite of forward transport in terms of energy.

When solving the adjoint F-P equation, the adjoint flux everywhere in the phantom is obtained. The input flux for the forward calculations can be determined using the gradient descent method. The gradient descent method (Section 3.4) is a first-order optimization method that uses the steepest gradient of an objective function to calculate new optimization variables at each iteration. However, convergence is often found at a local minimum instead of a global minimum. The gradient can be computed by only using the adjoint flux on the boundary.

3.2 Perturbation analysis

Perturbation analysis shows how a perturbation in one of the parameters causes a change in the response. This perturbation analysis can help determining important variables such as the adjoint source s^\dagger .

The response R is given in Equation (3.15). Σ_d is the detector response, which converts flux to dose.

$$R = \langle \Sigma_d, \phi \rangle . \quad (3.15)$$

A perturbation ΔR is added to the response in Equation (3.16):

$$\begin{aligned} R_0 + \Delta R = & \langle (\Sigma_d + \Delta\Sigma_d), (\phi_0 + \Delta\phi) \rangle = \\ & \langle \Sigma_d, \phi_0 \rangle + \langle \Sigma_d, \Delta\phi \rangle + \langle \Delta\Sigma_d, \phi_0 \rangle + \langle \Delta\Sigma_d, \Delta\phi \rangle . \end{aligned} \quad (3.16)$$

Note that the first term is just R_0 . If the second order term is neglected, an expression for ΔR is found:

$$\Delta R = \langle \Sigma_d, \Delta\phi \rangle + \langle \Delta\Sigma_d, \phi_0 \rangle . \quad (3.17)$$

A perturbation in the operator of the Fokker-Planck approximation and the flux leads to:

$$(L + \Delta L)(\phi_0 + \Delta\phi_0) = s. \quad (3.18)$$

Expanding the brackets, neglecting the second order term and removing the reference term $L\phi_0 = s$ gives:

$$\Delta L\phi_0 + L\Delta\phi_0 = 0. \quad (3.19)$$

The adjoint definition is applied in combination with Equation (3.19) to form:

$$\langle L^\dagger\phi^\dagger, \Delta\phi \rangle = - \langle \phi^\dagger, \Delta L\phi_0 \rangle. \quad (3.20)$$

The left-hand side of Equation (3.20) is equal to the second term of Equation (3.17) if the following condition holds:

$$L^\dagger\phi^\dagger = \Sigma_d. \quad (3.21)$$

The variation in the response can now be written as:

$$\Delta R = - \langle \phi^\dagger, \Delta L\phi \rangle + \langle \Delta\Sigma_d, \phi_0 \rangle. \quad (3.22)$$

Both inner products contain only the unperturbed flux ϕ and perturbations in operators. The change in response can thus be calculated without computing the transport equation for a perturbed state.

3.3 Adjoint source formulation

It is found that the adjoint source equals the detector function, when Equations (3.2) and (3.21) are combined. This is formulated in Equation (3.23):

$$\Sigma_d = s^\dagger. \quad (3.23)$$

Therefore, each type of response has a different adjoint source and a different solution of the adjoint flux. The Gateaux differential of a response is taken to calculate the adjoint source. A variation in the response due to a change in the flux can be calculated with the Gateaux derivative:

$$\Delta R = \lim_{\tau \rightarrow 0} \frac{R(\phi_0 + \tau\Delta\phi) - R(\phi_0)}{\tau}. \quad (3.24)$$

The contribution of the indirect effect on the variation in response is:

$$\Delta R = \langle \Sigma_d, \Delta\phi \rangle = \langle s^\dagger, \Delta\phi \rangle. \quad (3.25)$$

s^\dagger can now be determined using Equations (3.24) and (3.25).

In this research, an optimal set of beam angles and beam weights is chosen according to the least squares difference between deposited dose and prescribed dose. The objective function is written in Equation (3.26):

$$R = \min \sum_i w_i \cdot (D_i - D_{p,i})^2. \quad (3.26)$$

The delivered dose in voxel i is denoted by D_i and the prescribed dose in voxel i is given by $D_{p,i}$. w_i is the tissue weight of voxel i . The least squares difference is chosen, since it is a standard approach in regression analysis. Besides, it can be differentiated analytically. The weight of the tissue is included to give organ tissue, which is more vulnerable to irradiation, a higher importance than normal tissue, for example.

The flux to dose conversion is written in Equation (3.27), which equals the detector response function:

$$D(\mathbf{r}) = \int_E S^*(\mathbf{r}, E) \phi(\mathbf{r}, E) dE. \quad (3.27)$$

The adjoint source for the specific objective function and response function can now be derived. The objective function is again written in Equation (3.28), but now a reference state ϕ_0 is included:

$$R(\phi_0) = \sum_i w_i \cdot (D_i(\phi_0) - D_{p,i})^2. \quad (3.28)$$

A small perturbation $\tau \Delta \phi$ is added to the reference state ϕ_0 . This results in Equation (3.29). The perturbation is approximated by taking the first term of the Taylor expansion to simplify dose calculations:

$$R(\phi_0 + \tau \Delta \phi) = \sum_i w_i \cdot (D_i(\phi_0 + \tau \Delta \phi) - D_{p,i})^2 \approx \sum_i w_i \cdot \left(D_i(\phi_0) + \left. \frac{\partial D_i}{\partial \phi} \right|_{\phi_0} \tau \Delta \phi - D_{p,i} \right)^2. \quad (3.29)$$

Then, the Gateaux derivative is applied:

$$\Delta R = \lim_{\tau \rightarrow 0} \frac{1}{\tau} \left[\sum_i w_i \cdot \left(D_i(\phi_0) + \left. \frac{\partial D_i}{\partial \phi} \right|_{\phi_0} \tau \Delta \phi - D_{p,i} \right)^2 - \sum_i w_i \cdot (D_i(\phi_0) - D_{p,i})^2 \right]. \quad (3.30)$$

In Equation (3.31) the squares are written out:

$$\Delta R = \lim_{\tau \rightarrow 0} \frac{1}{\tau} \sum_i w_i \cdot \left[2D_i(\phi_0) \frac{\partial D_i}{\partial \phi} \Big|_{\phi_0} \tau \Delta \phi + \left(\frac{\partial D_i}{\partial \phi} \Big|_{\phi_0} \tau \Delta \phi \right)^2 - 2D_{p,i} \frac{\partial D_i}{\partial \phi} \Big|_{\phi_0} \tau \Delta \phi \right]. \quad (3.31)$$

Then, the limit τ to 0 is taken:

$$\Delta R = 2 \sum_i w_i \cdot \left[D_i(\phi_0) \frac{\partial D_i}{\partial \phi} \Big|_{\phi_0} \Delta \phi - D_{p,i} \frac{\partial D_i}{\partial \phi} \Big|_{\phi_0} \Delta \phi \right]. \quad (3.32)$$

The partial term $\frac{\partial D_i}{\partial \phi} \Big|_{\phi_0}$ can be rewritten by taking the derivative with respect to ϕ of Equation (3.27). The result is:

$$\frac{\partial D_i}{\partial \phi} \Big|_{\phi_0} = \int_E dE \cdot S_i^*(\mathbf{r}, E). \quad (3.33)$$

This term is substituted in Equation (3.32), which results in:

$$\begin{aligned} \Delta R &= 2 \sum_i w_i \cdot \left[D_i(\phi_0) \int_E dE \cdot S_i^*(\mathbf{r}, E) \Delta \phi - D_{p,i} \int_E dE \cdot S_i^*(\mathbf{r}, E) \Delta \phi \right] \\ &= 2 \sum_i w_i \cdot [D_i(\phi_0) - D_{p,i}] \int_E dE \cdot S_i^*(\mathbf{r}, E) \Delta \phi. \end{aligned} \quad (3.34)$$

Therefore, since $\Delta R = \langle s^\dagger, \Delta \phi \rangle$ (Equation (3.25)), the adjoint source is the following:

$$s^\dagger = 2 \sum_i w_i \cdot S_i^*(\mathbf{r}, E) [D_i(\phi_0) - D_{p,i}]. \quad (3.35)$$

The adjoint source can thus be written as the tissue weight multiplied by the stopping power and the dose difference. This is then summed over all voxels.

3.4 Gradient descent optimization

The gradient descent method uses the steepest gradient to improve the objective value. Based on the adjoint solution, an equation for the gradient can be found. The gradient can be computed using only the flux on the boundary. A transport problem is considered with boundary conditions described in Equation (3.36):

$$\phi(\mathbf{r}, E, \hat{\Omega}) = g(\mathbf{r}, \hat{\Omega}), \quad \hat{\Omega} \cdot n < 0. \quad (3.36)$$

A perturbation in the detector response can be written as integral over the boundary, the energy and the direction of all beams. This is done in Equation (3.37) [19]:

$$\Delta R = \int_{\partial V} \int_0^\infty \int_{\hat{\Omega} \cdot n < 0} \Delta g(\mathbf{r}, \hat{\Omega}) \phi^\dagger(\mathbf{r}, \hat{\Omega}) (\hat{\Omega} \cdot n) d\mathbf{r} dE d\hat{\Omega}. \quad (3.37)$$

The next step is to derive the gradient of this perturbation in the detector response in discrete form:

$$\frac{d\Delta R}{dg_{o,g,A,E}(\mathbf{r}, \hat{\Omega})} = A_{o,g,A,E}(\mathbf{r}, \hat{\Omega}). \quad (3.38)$$

Here, the subscripts o, g, A, E denote the ordinate, group number, average flux value, and average slope value respectively. Therefore, an expression in the form as given in Equation (3.39) is desired:

$$\Delta R = \sum_{o,g,A,E} A_{o,g,A,E}(\mathbf{r}, \hat{\Omega}) \cdot g_{o,g,A,E}(\mathbf{r}, \hat{\Omega}). \quad (3.39)$$

First, Equation (3.37) can easily be rewritten with (discrete) sums for the ordinates and the energy groups. This leads to:

$$\Delta R = \sum_g \sum_o w_o \int_g \int_{f, \partial V} \Delta g_{g,o}(\mathbf{r}, \hat{\Omega}) \phi_{g,o}^*(\mathbf{r}, \hat{\Omega}) (\hat{\Omega}_o \cdot n) d\mathbf{r} dE, \quad \hat{\Omega}_o \cdot n < 0. \quad (3.40)$$

Now, the energy needs to be rewritten in terms of the average and the slope values. The fluxes can be rewritten as:

$$\begin{aligned} \phi_{g,o}(E) &= \phi_{A,g,o} h^A(E) + \phi_{E,g,o} h^E(E), \\ \phi_{g,o}^*(E) &= \phi_{A,g,o}^* h^A(E) + \phi_{E,g,o}^* h^E(E), \\ \Delta g_{g,o}(E) &= \Delta g_{A,g,o} h^A(E) + \Delta g_{E,g,o} h^E(E). \end{aligned} \quad (3.41)$$

Substitution of $\phi_{g,o}^\dagger$ and $\Delta g_{g,o}$ results in:

$$\begin{aligned} \Delta R &= \sum_g \sum_o w_o \int_g \int_{f, \partial V} \left(\Delta g_{A,g,o}(\mathbf{r}, \hat{\Omega}) h^A(E) + \Delta g_{E,g,o}(\mathbf{r}, \hat{\Omega}) h^E(E) \right) \cdot \\ &\left(\phi_{A,g,o}^*(\mathbf{r}, \hat{\Omega}) h^A(E) + \phi_{E,g,o}^*(\mathbf{r}, \hat{\Omega}) h^E(E) \right) (\hat{\Omega}_o \cdot n) d\mathbf{r} dE, \quad \hat{\Omega}_o \cdot n < 0. \end{aligned} \quad (3.42)$$

The product $\phi_{g,o}^\dagger \cdot \Delta g_{g,o}$ is written out:

$$\begin{aligned} & \left(\Delta g_{A,g,o}(\mathbf{r}, \hat{\Omega}) h^A(E) + \Delta g_{E,g,o}(\mathbf{r}, \hat{\Omega}) h^E(E) \right) \cdot \\ & \left(\phi_{A,g,o}^*(\mathbf{r}, \hat{\Omega}) h^A(E) + \phi_{E,g,o}^*(\mathbf{r}, \hat{\Omega}) h^E(E) \right) = \\ & \Delta g_{A,g,o}(\mathbf{r}, \hat{\Omega}) h^A(E) \phi_{A,g,o}^*(\mathbf{r}, \hat{\Omega}) h^A(E) + \Delta g_{A,g,o}(\mathbf{r}, \hat{\Omega}) h^A(E) \phi_{E,g,o}^*(\mathbf{r}, \hat{\Omega}) h^E(E) + \\ & \Delta g_{E,g,o}(\mathbf{r}, \hat{\Omega}) h^E(E) \phi_{A,g,o}^*(\mathbf{r}, \hat{\Omega}) h^A(E) + \Delta g_{E,g,o}(\mathbf{r}, \hat{\Omega}) h^E(E) \phi_{E,g,o}^*(\mathbf{r}, \hat{\Omega}) h^E(E). \end{aligned} \quad (3.43)$$

Performing the integral over E and using the orthogonality property of the basis functions (Equation (2.10)) results in Equation (3.44):

$$\Delta g_{A,g,o}(\mathbf{r}, \hat{\Omega}) \phi_{A,g,o}^*(\mathbf{r}, \hat{\Omega}) \Delta E_g + \Delta g_{E,g,o}(\mathbf{r}, \hat{\Omega}) \phi_{E,g,o}^*(\mathbf{r}, \hat{\Omega}) \frac{\Delta E_g}{3}. \quad (3.44)$$

Substituting Equation (3.44) in the equation for ΔR (Equation (3.42)) gives:

$$\begin{aligned} \Delta R &= \sum_g \sum_o w_o \cdot \\ & \int_{f, \partial V} \left(\Delta g_{A,g,o}(\mathbf{r}, \hat{\Omega}) \phi_{A,g,o}^*(\mathbf{r}, \hat{\Omega}) \Delta E_g + \Delta g_{E,g,o}(\mathbf{r}, \hat{\Omega}) \phi_{E,g,o}^*(\mathbf{r}, \hat{\Omega}) \frac{\Delta E_g}{3} \right) \cdot \\ & (\hat{\Omega}_o \cdot n) d\mathbf{r}, \quad \hat{\Omega}_o \cdot n < 0. \end{aligned} \quad (3.45)$$

The last integral becomes a sum over the cell faces. A_f represents the area of cell face f , $f = 1, \dots, n_f$, ($\int_{f, \partial V} d\mathbf{r} = \sum_f A_f$). This is done in Equation (3.46):

$$\begin{aligned} \Delta R &= \sum_g \sum_o w_o \sum_f A_f \cdot \\ & \left(\Delta g_{A,g,o,f}(\mathbf{r}, \hat{\Omega}) \phi_{A,g,o,f}^*(\mathbf{r}, \hat{\Omega}) \Delta E_g + \Delta g_{E,g,o,f}(\mathbf{r}, \hat{\Omega}) \phi_{E,g,o,f}^*(\mathbf{r}, \hat{\Omega}) \frac{\Delta E_g}{3} \right) \cdot \\ & (\hat{\Omega}_o \cdot n), \quad \hat{\Omega}_o \cdot n < 0. \end{aligned} \quad (3.46)$$

From here, $A_{o,g,A,E}(\mathbf{r}, \hat{\Omega})$ can be determined which forms the gradient. The input flux for forward transport is based on this gradient.

3.5 Adjoint discretization

To solve the adjoint transport equation, similar discretizations (energy, domain and operators) have to be done as for forward transport. The energy and spatial domain discretizations are comparable to the discretizations of forward transport, since only the adjoint operators are slightly changing. Sections 3.5.1 and 3.5.2 show the adjoint discretizations in the operators. The discretization of the adjoint source is treated in Section 3.5.3. Finally, the Crank-Nicolson method is explained for adjoint variables in Section 3.5.4.

3.5.1 Adjoint Continuous Slowing Down operator

The same recipe is used for the discretization of the adjoint CSD as for the forward CSD (Section 2.3.2). In Equation (3.47), the adjoint CSD operator is rewritten:

$$L_{CSD}^\dagger(\cdot) = -S^*(\mathbf{r}, E) \frac{\partial}{\partial E}(\cdot). \quad (3.47)$$

The adjoint flux can be expanded as is done in Equation (3.48):

$$\phi^\dagger(\mathbf{r}, E) = \phi_g^{\dagger 0}(\mathbf{r}) h_g^0(E) + \phi_g^{\dagger 1}(\mathbf{r}) h_g^1(E). \quad (3.48)$$

The average part is obtained when multiplying the adjoint CSD operator with the first basis function $h^0(E)$ and integrating over the energy group. Equation (3.49) shows the result:

$$\begin{aligned} & \int_{E_{g+\frac{1}{2}}}^{E_{g-\frac{1}{2}}} -S^*(\mathbf{r}, E) \frac{\partial}{\partial E} \left(\phi^\dagger(\mathbf{r}, E) \right) h^0(E) dE = \\ & - \left[S^*(\mathbf{r}, E) \phi^\dagger(\mathbf{r}, E) h^0(E) \right]_{E_{g+\frac{1}{2}}}^{E_{g-\frac{1}{2}}} + \int_{E_{g+\frac{1}{2}}}^{E_{g-\frac{1}{2}}} \phi^\dagger(\mathbf{r}, E) \frac{\partial S^*(\mathbf{r}, E)}{\partial E} h^0(E) dE. \end{aligned} \quad (3.49)$$

The first term on the right hand side can be written as follows:

$$\begin{aligned} & - \left[S^*(\mathbf{r}, E) \phi^\dagger(\mathbf{r}, E) h^0(E) \right]_{E_{g+\frac{1}{2}}}^{E_{g-\frac{1}{2}}} = \\ & - S^*(\mathbf{r}, E_{g-\frac{1}{2}}) \left(\phi_{g-1}^{\dagger 0}(\mathbf{r}) + \phi_{g-1}^{\dagger 1}(\mathbf{r}) \right) + S^*(\mathbf{r}, E_{g+\frac{1}{2}}) \left(\phi_g^{\dagger 0}(\mathbf{r}) + \phi_g^{\dagger 1}(\mathbf{r}) \right). \end{aligned} \quad (3.50)$$

The integral term on the right side can be evaluated by approximating the derivative of the stopping power and expanding the adjoint flux. When applying the orthogonality condition, the following is obtained:

$$\begin{aligned}
& \int_{E_{g+\frac{1}{2}}}^{E_{g-\frac{1}{2}}} \phi^\dagger(\mathbf{r}, E) \frac{\partial S^*(\mathbf{r}, E)}{\partial E} h^0(E) dE = \\
& \int_{E_{g+\frac{1}{2}}}^{E_{g-\frac{1}{2}}} \frac{S^*(\mathbf{r}, E_{g-\frac{1}{2}}) - S^*(\mathbf{r}, E_{g+\frac{1}{2}})}{\Delta E_g} \left(\phi_g^{\dagger 0}(\mathbf{r}, E) h^0(E) + \phi_g^{\dagger 1}(\mathbf{r}, E) h^1(E) \right) h^0(E) dE = \\
& \left((S^*(\mathbf{r}, E_{g-\frac{1}{2}}) - S^*(\mathbf{r}, E_{g+\frac{1}{2}})) \phi_g^{\dagger 0}(\mathbf{r}) \right). \quad (3.51)
\end{aligned}$$

Now, an expression for the adjoint CSD operator multiplied with the first basis function can be formulated:

$$\begin{aligned}
& \int_{E_{g+\frac{1}{2}}}^{E_{g-\frac{1}{2}}} -S^*(\mathbf{r}, E) \frac{\partial}{\partial E} \left(\phi^\dagger(\mathbf{r}, E) \right) h^0(E) dE = \\
& S^*(\mathbf{r}, E_{g-\frac{1}{2}}) \phi^{\dagger 0}(\mathbf{r}, E_{g-\frac{1}{2}}) - S^*(\mathbf{r}, E_{g+\frac{1}{2}}) \phi^{\dagger 0}(\mathbf{r}, E_{g+\frac{1}{2}}) - \\
& S^*(\mathbf{r}, E_{g-\frac{1}{2}}) \left(\phi_{g-1}^{\dagger 0}(\mathbf{r}) + \phi_{g-1}^{\dagger 1}(\mathbf{r}) \right) + S^*(\mathbf{r}, E_{g+\frac{1}{2}}) \left(\phi_g^{\dagger 0}(\mathbf{r}) + \phi_g^{\dagger 1}(\mathbf{r}) \right). \quad (3.52)
\end{aligned}$$

Equation (3.53) is obtained when multiplying Equation (3.47) with the second basis function $h^1(E)$ and integrating over an energy group:

$$\begin{aligned}
& \int_{E_{g+\frac{1}{2}}}^{E_{g-\frac{1}{2}}} -S^*(\mathbf{r}, E) \frac{\partial}{\partial E} \left(\phi^\dagger(\mathbf{r}, E) \right) h^1(E) dE = \\
& - \left[S^*(\mathbf{r}, E) \phi^\dagger(\mathbf{r}, E) h^1(E) \right]_{E_{g+\frac{1}{2}}}^{E_{g-\frac{1}{2}}} + \int_{E_{g+\frac{1}{2}}}^{E_{g-\frac{1}{2}}} \phi^\dagger(\mathbf{r}, E) \frac{\partial S^*(\mathbf{r}, E) h^1(E)}{\partial E} dE. \quad (3.53)
\end{aligned}$$

Evaluating the integral on the right hand side gives:

$$\int_{E_{g+\frac{1}{2}}}^{E_{g-\frac{1}{2}}} \phi^\dagger(\mathbf{r}, E) h^1(E) \frac{\partial S^*(\mathbf{r}, E)}{\partial E} dE + \int_{E_{g+\frac{1}{2}}}^{E_{g-\frac{1}{2}}} \phi^\dagger(\mathbf{r}, E) S^*(\mathbf{r}, E) \frac{\partial h^1(E)}{\partial E} dE. \quad (3.54)$$

If the adjoint flux and stopping power coefficient are expanded and the orthogonality condition is applied, Equation (3.55) is obtained for the first integral of Equation (3.54):

$$\frac{S^*(\mathbf{r}, E_{g-\frac{1}{2}}) + S^*(\mathbf{r}, E_{g+\frac{1}{2}})}{3} \phi_g^{\dagger 1}(\mathbf{r}, E). \quad (3.55)$$

Expanding the adjoint flux and the stopping power coefficient in terms of the basis functions for the second integral of Equation (3.54) and applying the orthogonality condition results in:

$$\left(S^*(\mathbf{r}, E_{g-\frac{1}{2}}) + S^*(\mathbf{r}, E_{g+\frac{1}{2}}) \right) \phi_g^{\dagger 0}(\mathbf{r}, E) + \frac{S^*(\mathbf{r}, E_{g-\frac{1}{2}}) + S^*(\mathbf{r}, E_{g+\frac{1}{2}})}{3} \phi_g^{\dagger 1}(\mathbf{r}, E). \quad (3.56)$$

The first term of Equation (3.53) can be evaluated as follows:

$$\begin{aligned} & - \left[S^*(\mathbf{r}, E) \phi^{\dagger}(\mathbf{r}, E) h^1(E) \right]_{E_{g+\frac{1}{2}}}^{E_{g-\frac{1}{2}}} = \\ & - S^*(\mathbf{r}, E_{g-\frac{1}{2}}) \left(\phi_g^{\dagger 0}(\mathbf{r}, E) + \phi_g^{\dagger 1}(\mathbf{r}, E) \right) - S^*(\mathbf{r}, E_{g+\frac{1}{2}}) \left(\phi_{g+1}^{\dagger 0}(\mathbf{r}, E) + \phi_{g+1}^{\dagger 1}(\mathbf{r}, E) \right). \end{aligned} \quad (3.57)$$

The total result for the slope part is given in Equation (3.58):

$$\begin{aligned} & \int_{E_{g+\frac{1}{2}}}^{E_{g-\frac{1}{2}}} -S^*(\mathbf{r}, E) \frac{\partial}{\partial E} \left(\phi^{\dagger}(\mathbf{r}, E) \right) h^1(E) dE = \\ & \frac{2}{3} \left(S^*(\mathbf{r}, E_{g-\frac{1}{2}}) + S(\mathbf{r}, E_{g+\frac{1}{2}}) \right) \phi_g^{\dagger 1}(\mathbf{r}, E) + \left(S^*(\mathbf{r}, E_{g-\frac{1}{2}}) + S^*(\mathbf{r}, E_{g+\frac{1}{2}}) \right) \phi_g^{\dagger 0}(\mathbf{r}, E) \\ & - S^*(\mathbf{r}, E_{g-\frac{1}{2}}) \left(\phi_g^{\dagger 0}(\mathbf{r}, E) + \phi_g^{\dagger 1}(\mathbf{r}, E) \right) - S^*(\mathbf{r}, E_{g+\frac{1}{2}}) \left(\phi_{g+1}^{\dagger 0}(\mathbf{r}, E) + \phi_{g+1}^{\dagger 1}(\mathbf{r}, E) \right). \end{aligned} \quad (3.58)$$

Equations (3.52) and (3.58) can be used to solve the adjoint Fokker-Planck approximation numerically using the C-N method.

3.5.2 Adjoint Straggling operator

Since the straggling operator and its adjoint operator are the same (self-adjoint, see Equation (3.12)), the discretizations in the forward and the adjoint case are equal.

3.5.3 Adjoint source

The adjoint source (Equation (3.35)) contains the stopping power coefficient. The discretizations (in energy and spatial domain) are therefore based on the stopping power, which are the same as for the CSD operator, where the stopping power is used. The adjoint source is used as initial condition for adjoint transport. The initial condition is represented as a δ -function at the centre of a voxel. This is done for all voxels to form the complete adjoint source.

3.5.4 Crank-Nicolson - adjoint

A set of linear equations, given in Equation (3.59), is obtained after discretizing the energy domain:

$$-\frac{d\phi^\dagger(\mathbf{r})}{dz} = L^\dagger(\mathbf{r})\phi^\dagger(\mathbf{r}). \quad (3.59)$$

$\phi^\dagger(\mathbf{r})$ is written as a combination of the average and slope for each energy group, $\phi^\dagger(\mathbf{r}) = [\phi_1^{\dagger 0}(\mathbf{r}), \phi_1^{\dagger 1}(\mathbf{r}) \dots \phi_g^{\dagger 0}(\mathbf{r}), \phi_g^{\dagger 1}(\mathbf{r}) \dots \phi_{NG}^{\dagger 0}(\mathbf{r}), \phi_{NG}^{\dagger 1}(\mathbf{r})]^T$, with NG the number of groups. $L^\dagger(\mathbf{r})$ contains all variables of the operators in the adjoint Fokker-Planck equation in a matrix. The minus sign implies that the protons are flowing in opposite direction of $\hat{\Omega}$. $\phi^\dagger(\mathbf{r})$ is independent of E from now on. The Crank-Nicolson method uses the same steps for the adjoint as is done for the forward method in Section 2.3.4.

The spatial domain of the phantom is again divided into voxels. For the adjoint case, each voxel is bounded to a number of directions, which form rays. These directions are equally spaced distributed over a sphere. The rays start at the center of a voxel and end at the boundary of the phantom in the adjoint case. When rays end at the same boundary position and have the same direction, the rays can be summed to beams to reduce the amount of total beams that has to be computed in the forward case. Rays that do not have influence on tumor voxels are also left out in the computations to speed up the process. This can speed up the calculations by a factor 100.

The finite difference approximation is now the following:

$$-\frac{d\phi^\dagger(z_{i+\frac{1}{2}})}{dz} \approx \frac{\phi^\dagger(\mathbf{r}_{i+1}) - \phi^\dagger(\mathbf{r}_i)}{z_i - z_{i+1}}. \quad (3.60)$$

Similarly to the forward method, the following approximation can be done:

$$L^\dagger(z_{i+\frac{1}{2}})\phi^\dagger(z_{i+\frac{1}{2}}) \approx \frac{1}{2} \left(L^\dagger(\mathbf{r}_i)\phi^\dagger(\mathbf{r}_i) + L^\dagger(\mathbf{r}_{i+1})\phi^\dagger(\mathbf{r}_{i+1}) \right). \quad (3.61)$$

This leads to Equation (3.62), if $L^\dagger(\mathbf{r})$ is assumed to be constant within a cell:

$$\frac{\phi^\dagger(\mathbf{r}_{i+1}) - \phi^\dagger(\mathbf{r}_i)}{z_i - z_{i+1}} = \frac{1}{2} L^\dagger(z_{i+\frac{1}{2}}) \cdot \left(\phi^\dagger(\mathbf{r}_i) + \phi^\dagger(\mathbf{r}_{i+1}) \right). \quad (3.62)$$

Equation (3.62) can now be written in recursive form:

$$\phi^\dagger(\mathbf{r}_{i+1}) = \frac{1 + \frac{1}{2} L^\dagger(z_{i+\frac{1}{2}})(z_i - z_{i+1})}{1 - \frac{1}{2} L^\dagger(z_{i+\frac{1}{2}})(z_i - z_{i+1})} \phi^\dagger(\mathbf{r}_i). \quad (3.63)$$

$\phi^\dagger(\mathbf{r}_i)$ is already known, because of the initial boundary conditions. Therefore, $\phi^\dagger(\mathbf{r}_{i+1})$ can be calculated using Equation (3.63).

3.6 Beam angle selection

The optimal beam angle selection with beam weights can be found using an iteration scheme. A flow diagram with the corresponding steps is given in Figure 6. Two programming environments are used, Matlab [14] and Fortran, which exchange data with each other.

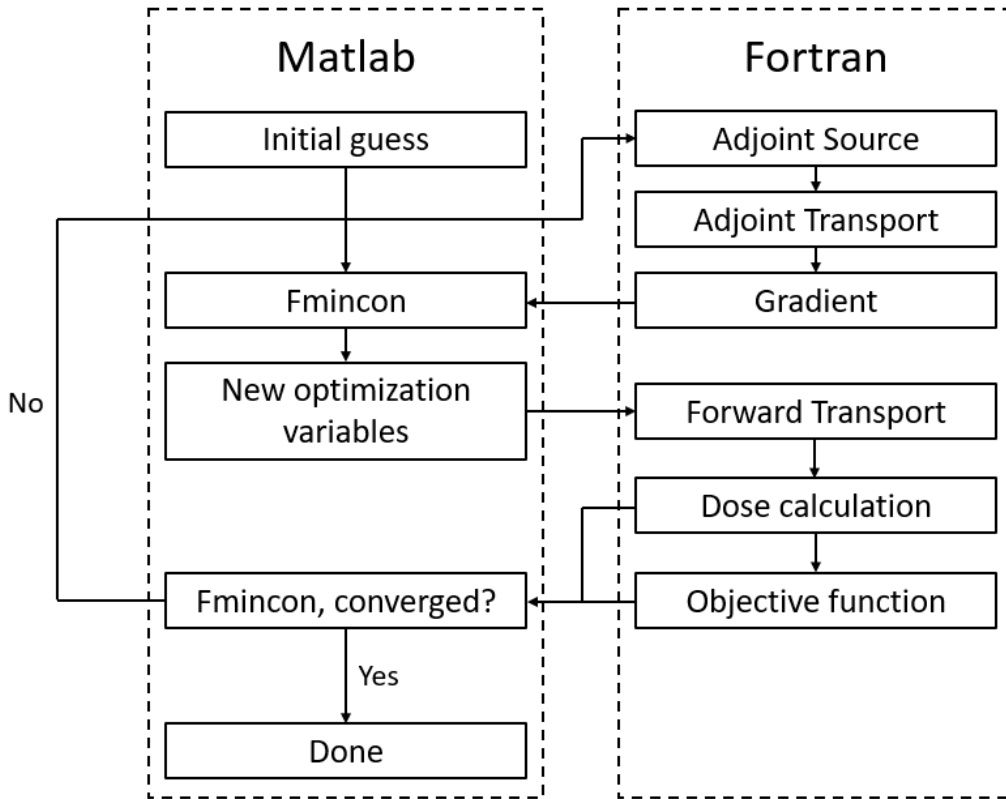


Figure 6: A flow diagram with the needed steps to perform the adjoint method computations. The calculations are done within the Matlab and the Fortran environment.

First, an initial guess ϕ_0 is made for all coefficients of ϕ . Within the Fortran environment, a predefined selection of possible beams should be provided as well. Then, a solver called 'Fmincon' (Find MINimum of CONstrained nonlinear multivariable function) within programming language Matlab [14] calls the Fortran environment to run forward transport using the initial guess. This results in a dose distribution and an objective value. Both are passed back to fmincon within the Matlab environment. Fmincon checks if convergence or any tolerance limits are reached. If this is not the case, the dose values are passed to Fortran to calculate an adjoint source. The adjoint source is used in adjoint transport, which results in a gradient using the gradient descent method. Then, a new set of optimization variables, while obeying a non-negativity constraint, can be determined within fmincon. This is passed to Fortran to compute the new dose distribution and objective value. The scheme can be iterated till convergence is reached.

Since the gradient and flux input are connected to every beam, the output is an optimal set of flux coefficients for all beams at all energies. The objective value and the dose distribution can also be plotted. If desired, a maximum number of iterations can be set.

4 Results

This chapter describes the results of the adjoint method for beam angle optimization. Section 4.1 shows an overview of the set-up. All parameters and a figure of the phantom and beams are given. Specific implementation details and a validation for the energy are explained in Section 4.2. The objective function values are given in Section 4.3. The dose distribution is shown in Section 4.4 and the input flux and gradient of the beams are given in Section 4.5. Finally, results for higher numbers of directions are displayed in Section 4.6.

4.1 Set-up

Figure 7 illustrates the geometry of the phantom used in the computations. The voxel number is displayed on the x -, y -, and z -axis. A single voxel has a $2 \times 2 \times 2$ cm size. Brown voxels simulate a tumor. Blue voxels represent organs. Water is surrounding the tumor and organs to mimic normal tissue.

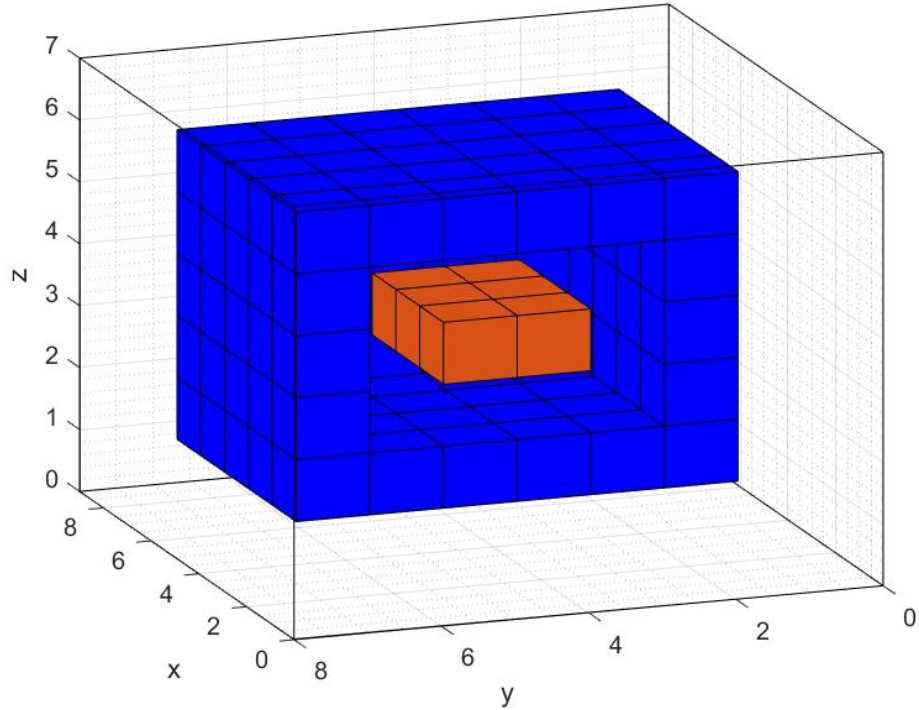


Figure 7: An illustration of the phantom used in the computations. The tumor is represented by brown voxels and organs are given by blue voxels. Around the tumor and organs water is present. Each voxel has a $2 \times 2 \times 2$ cm size. The voxel number is given on the x -, y -, and z -axis.

In total, 6 tumor voxels, 102 organ voxels, and 396 water voxels are present, respectively. The tumor voxels are defined at $x \in [4, 6]$, $y \in [4, 5]$, $z \in [4]$. All tumor voxels have 1 water voxel in front of an organ voxel. Figures 8 and 9 represent cross-sections in the xy -plane at $z = 3.5$ and the xz -plane at $y = 4$, respectively.

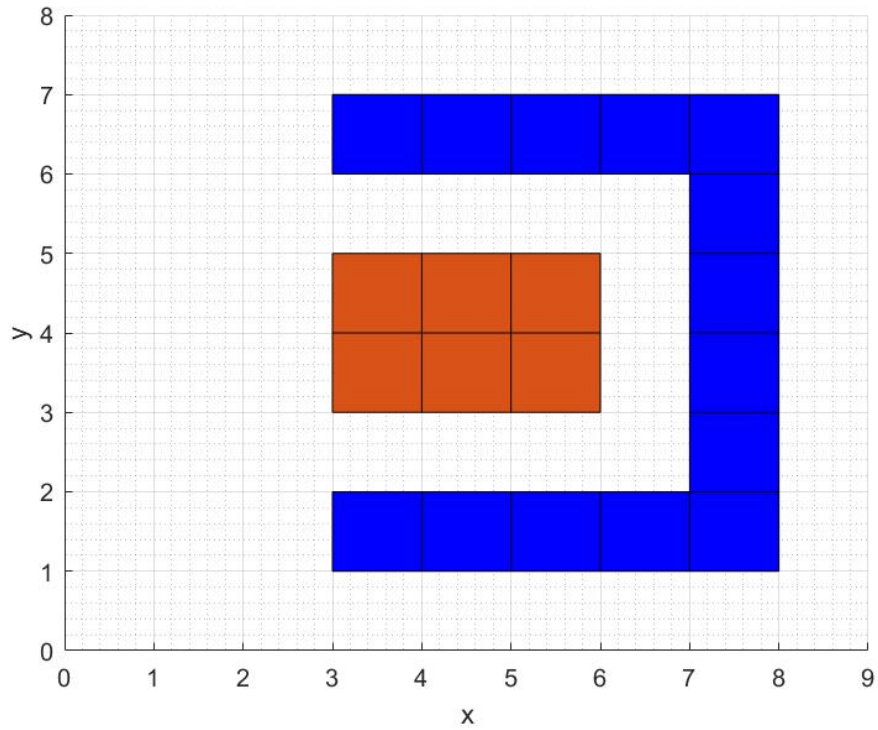


Figure 8: A xy cross-section of the phantom. The tumor is represented by brown voxels and organs are given by blue voxels. Around the tumor and organs water is present. Each voxel has a $2 \times 2 \times 2$ cm size. The voxel number is given on the x - and y -axis.

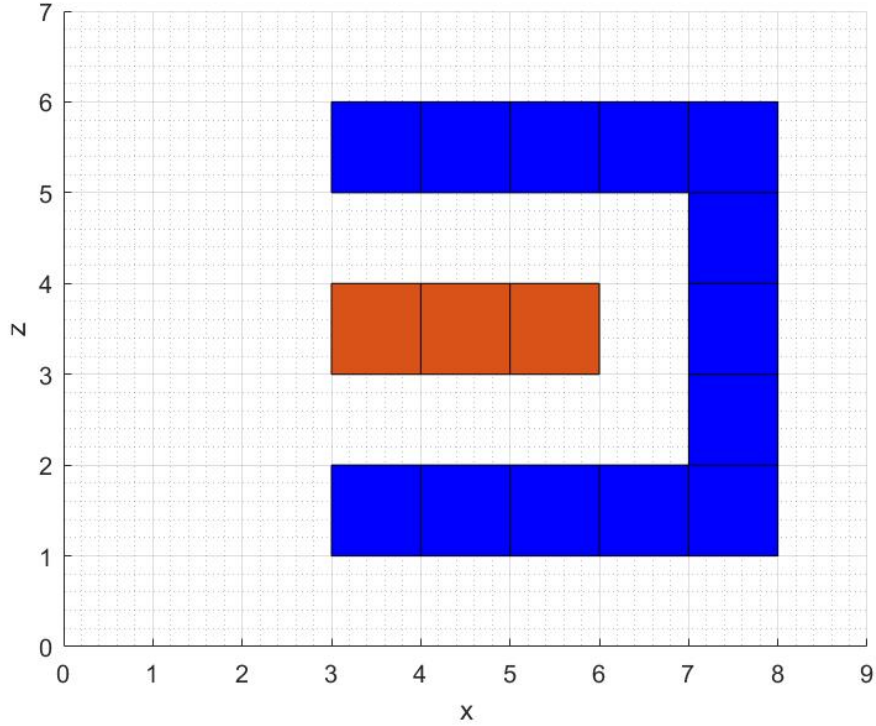


Figure 9: A xz cross-section of the phantom. The tumor is represented by brown voxels and organs are given by blue voxels. Around the tumor and organs water is present. Each voxel has a $2 \times 2 \times 2$ cm size. The voxel number is given on the x - and z -axis.

Table 1 contains all parameter values used in the adjoint method computation. Furthermore, the initial flux input equals $\phi_0 = 0$. A dose of 60 MeV cm^{-3} has to be deposited in tumor voxels. Only two beam directions are possible: \hat{x} and $-\hat{x}$. These are plotted and numbered in Figure 10.

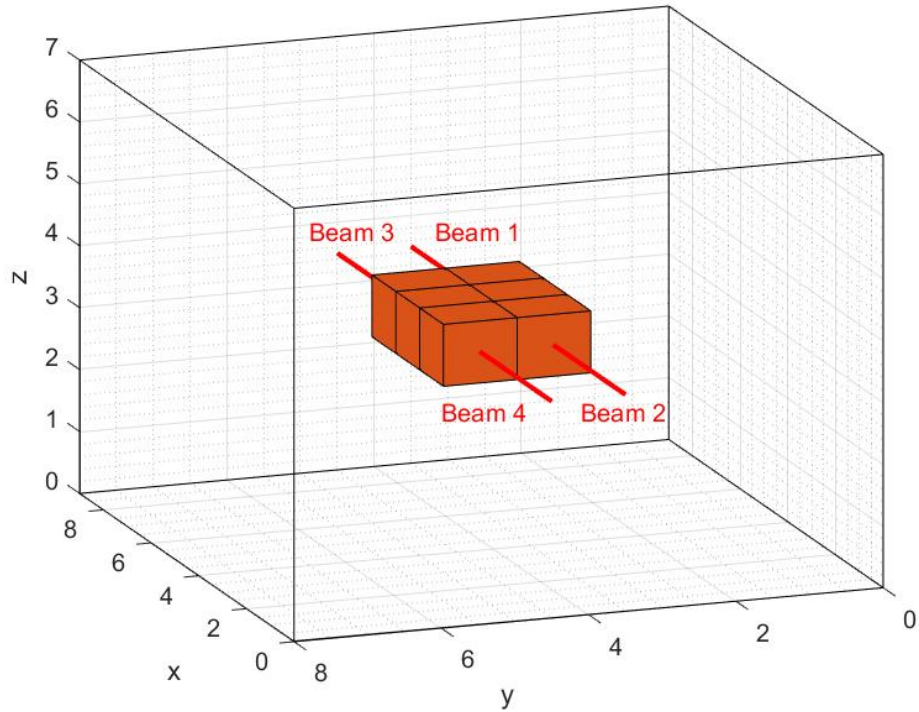


Figure 10: An illustration of the directions of the important beams for the set-up. The beams are numbered. Beams 1 and 3 first cross organs, beams 2 and 4 first cross water before reaching the tumor. The organ voxels have been left out for clarity.

The maximum energy is set to 176 MeV, which is high enough to cover the whole phantom in the \hat{x} direction (= 18 cm). The `fmincon` solver in Matlab has a few options for the Hessian approximation. The LBFGS algorithm (limited-memory Broyden–Fletcher–Goldfarb–Shanno algorithm) is chosen, since it can deal with large-scale problems, while it uses little memory. The algorithm is then still able to run, if the number of optimization variables becomes very high for large problems.

Table 1: An overview of all parameters used in the adjoint method computation. A dose of 60 MeV cm^{-3} has to be deposited in tumor voxels.

Voxels	504
E_{min}	1 MeV
E_{max}	176 MeV
Energy groups	175
Energy group width	1 MeV
Possible directions	2
Hessian approximation	LBFGS
Water weight	1
Tumor weight	10
Organ weight	100
Prescribed water dose	0 MeV cm^{-3}
Prescribed tumor dose	60 MeV cm^{-3}
Prescribed organ dose	0 MeV cm^{-3}
Spatial stepsize	0.01 cm
Stepsize tolerance	$1.0 \cdot 10^{-10}$

A relatively high organ weight is used to make sure the algorithm really tries to avoid organs. The tumor weight is still high enough to ensure dose will be deposited in the tumor. Therefore, the initial guess is not the optimal solution. The spatial stepsize is set to 0.01 cm. A smaller stepsize increases the computation time, but leads to more accuracy.

4.2 Validation

The flux ϕ might become lower than zero for some energy groups during optimization. Therefore, a constraint is needed, since negative flux or dose is physically impossible. The flux ϕ is a combination of the average and slope coefficient (Equation (3.41)). If the flux ϕ on the boundary is lower than zero, the values of the coefficients are changed such that $\phi \geq 0$. This is done by calculating the flux at the boundaries of a group (here, the flux always has the lowest and highest value within an energy group) and setting the flux to zero, if the calculated flux at a boundary point (might also be both boundary points) is below zero, see Figure 11. The left side shows the original flux ϕ , the right side shows ϕ after applying the constraints. The coefficients for the average flux and the normalized slope of the flux are adjusted accordingly.

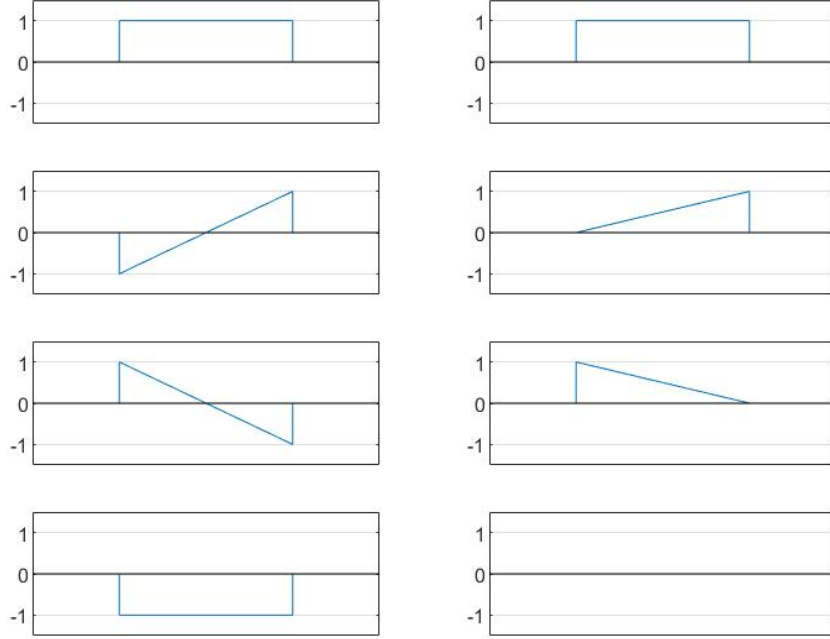


Figure 11: An overview of different scenarios for the flux ϕ for one energy group. On the left, the original flux ϕ is displayed. On the right, ϕ is displayed after making adjustments. If ϕ becomes lower than 0 on the boundary, the boundary value of an energy group is set to 0 and the slope is adjusted accordingly to make ϕ non-negative, i.e. $\phi \geq 0$.

Second, the input energy of the system should be equal to the deposited dose (if no energy is leaving the domain). Conservation of energy should always be true. Therefore, a check can be done. First, the total input energy is calculated using Equation (4.1):

$$E_{in} = \int_{E_{min}}^{E_{max}} E\phi_0(E)dE. \quad (4.1)$$

$\phi_0(E)$ contains the flux at the boundary for all energy groups and all beams. The computed value for the final iteration is $E_{in} = 4.8685757 \cdot 10^3$ MeV. The total deposited dose, calculated according to Section 2.4, equals $E = 4.8689645 \cdot 10^3$ MeV. The total energy leaving the domain is equal to zero

(as can be verified by looking to Figures 14 and 15). The difference is in the order of 10^{-1} MeV, which is insignificant for this problem. Therefore, energy is considered to be conserved.

4.3 Objective function

Table 2 shows the numerical results of the adjoint method computed with the parameters from Table 1. The objective value at iteration 0 equals $1.728 \cdot 10^6$. After 77 iterations, a final objective value of $8.12 \cdot 10^4$ is reached. The stepsize tolerance is reached and no significant improvement is made. A possible local minimum is found. The computations lasted 290 seconds.

Table 2: The numerical results of the adjoint method for the set-up described in Section 4.1.

Iterations	77
Final objective value	$8.12 \cdot 10^4$
Computation time	290 s

The objective value for each iteration is displayed in Figure 12. The objective value is decreasing at every step. A sharp decrease is present within the first iterations. This is caused by delivering dose in the tumor voxels. However, organs received some dose as well and have a relative high weight, which counteracts the decrease a bit. Then, the next step is to simultaneously avoid organs and deliver dose in tumor, which causes the sharpest decrease around iteration 4.

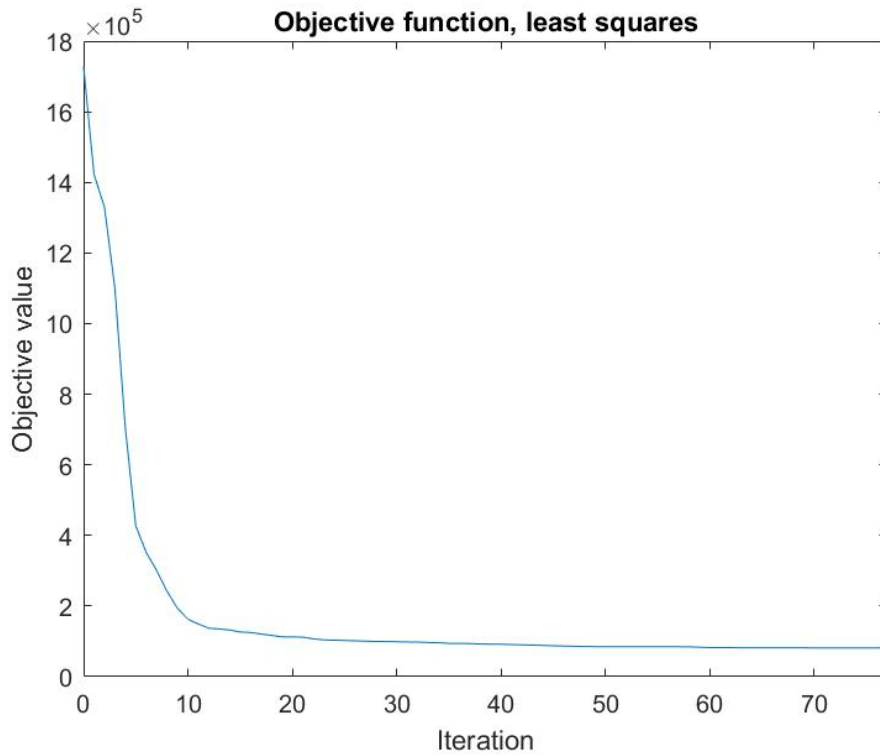


Figure 12: The objective function as function of iteration.

After iteration 20, it is slowly converging to a (local) minimum. Only minor improvements are made. It is impossible to reach an objective value of zero, since the protons first have to cross some water voxels before reaching the tumor.

4.4 Dose distribution

Figure 13 represents the final dose distribution. The tumor voxels are located in layer $z = 4$ and are surrounded by the red contour. The organ voxels are represented by the green contour. Since the beams point in the \hat{x} or $-\hat{x}$ direction, only layer $z = 4$ receives any dose.

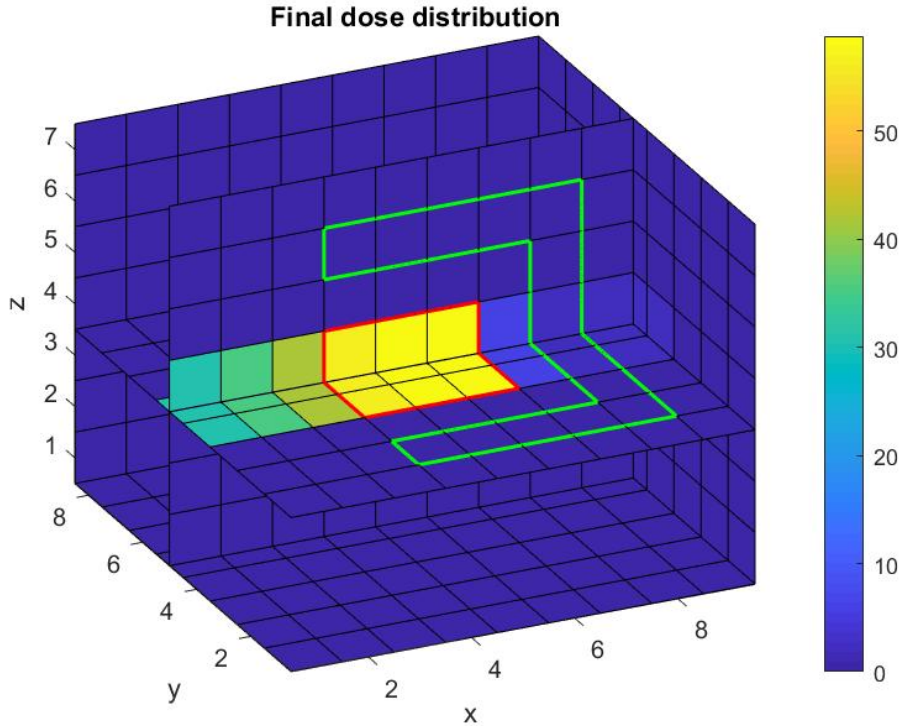


Figure 13: The final dose distribution. The tumor voxels are located in layer $z = 4$ and surrounded by the red contour. The organ voxels are represented by the green contour. The prescribed dose of 60 MeV cm^{-3} is nearly reached. The dose mainly comes from the left and avoids organ voxels.

The prescribed dose of 60 MeV cm^{-3} is nearly reached. The prescribed dose is not achieved completely, since the stepsize tolerance is reached in the optimization process. The dose mainly comes from the left and thus avoids organ voxels. However, some dose still comes from the right. This is to compensate for underdose in the tumor voxels. Furthermore, the dose deposition at the boundary voxels is higher than the dose deposition at the voxels more on the inside. This should not be the case and is caused by an error in the algorithm.

4.5 Forward flux

Figures 14 and 15 show the input flux for the four relevant beams, when ϕ is converged. Beams 1 and 3 cross organs before they reach the tumor, while

beams 2 and 4 only travel through water.

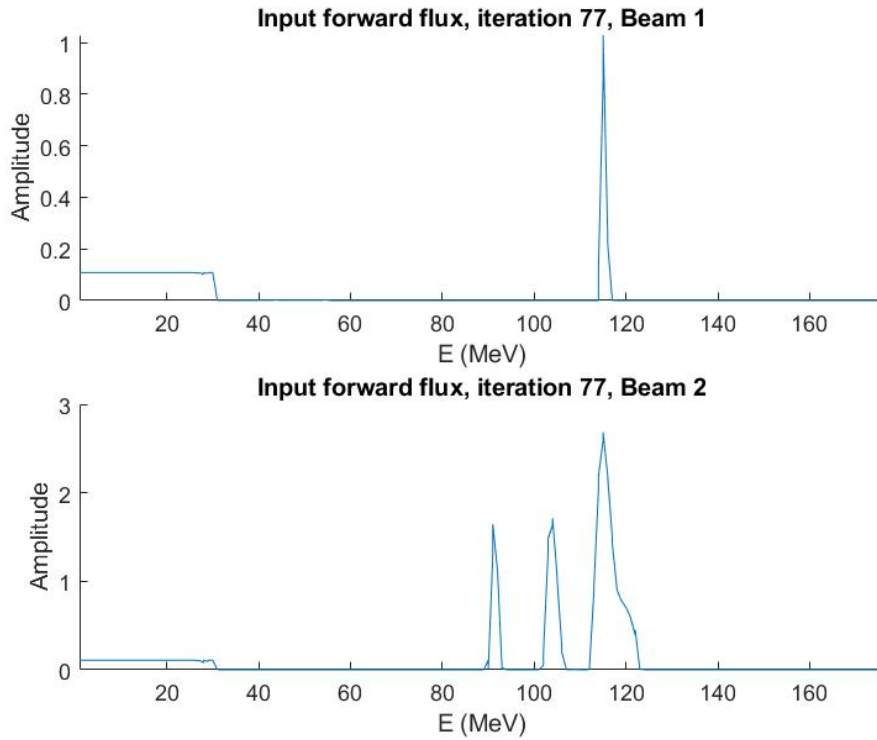


Figure 14: The input flux for beams 1 and 2 at iteration 77. Beam 1 crosses organs first, while beam 2 only goes through water. The peaks represent locations of tumor voxels. A non-zero amplitude is present at low energy.

Beams 1 and 3, and beams 2 and 4 have exactly the same input, because the phantom and corresponding beams are symmetric. The three peaks in the input flux for beams 2 and 4 correspond to the three tumor voxels in the $y = 4$ and $y = 5$ row. Apparently, the tumor voxels on the far left do not receive enough dose from beams 2 and 4. A small additional dose from the beams crossing organs first is needed to compensate the underdose.

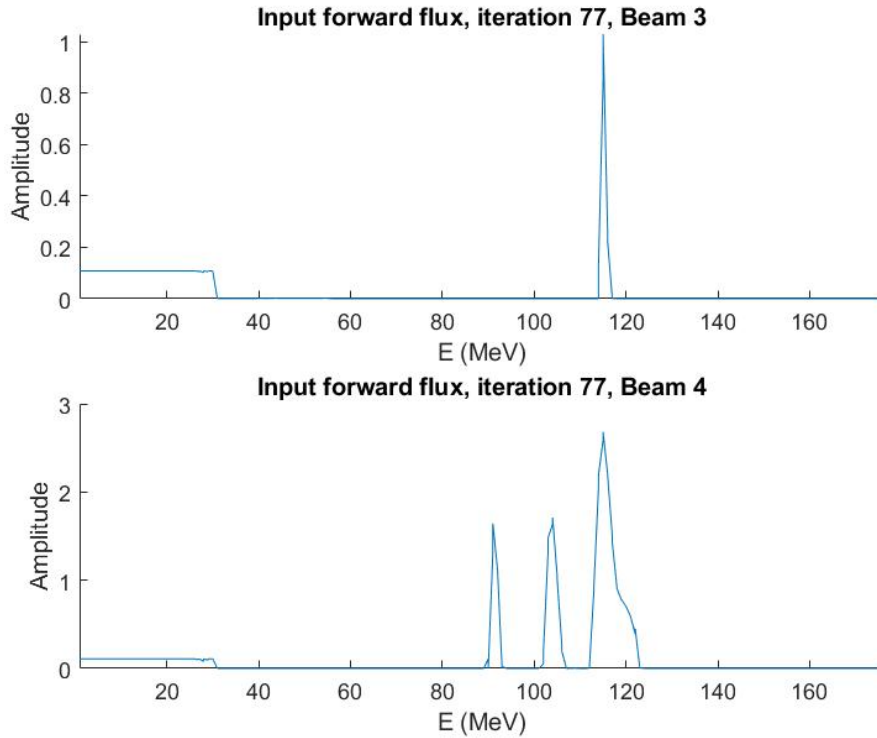


Figure 15: The input flux for beams 3 and 4 at iteration 77. Beam 3 crosses organs first, while beam 4 only goes through water. The peaks represent locations of tumor voxels. A non-zero amplitude is present at low energies.

All graphs in Figures 14 and 15 contain a small amplitude for the lowest energy groups. The algorithm wants to put the dose exactly in the middle of a voxel, due to the initial condition and discretization of the adjoint source (Section 3.5). Due to this discretization error, the first half voxel is ignored in gradient calculations. That is also the reason why there are peaks for the tumor voxels instead of bins.

Figures 16 and 17 show the gradient for the same four relevant beams, when ϕ is converged.

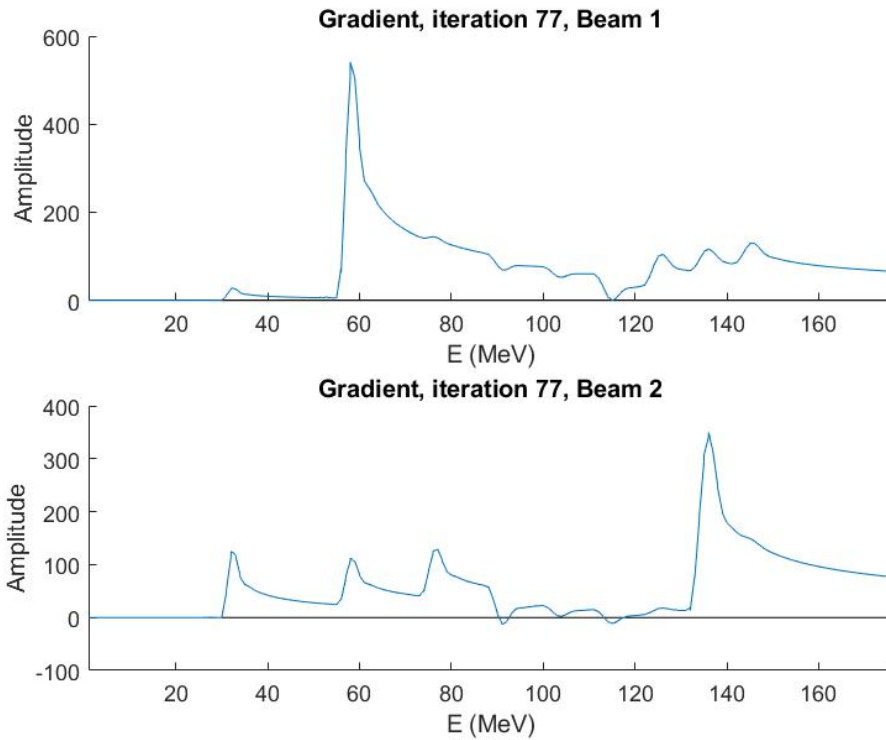


Figure 16: The gradient for beams 1 and 2 at iteration 77. The high peaks represent the location of organ voxels. The smaller upward peaks are connected to water voxels and downward peaks correspond to tumor voxels. The gradient is zero at low energies.

Beams 1 and 3, and beams 2 and 4 have again the same values. The largest upward peak corresponds to organ voxels (with a weight of 100). The other upward peaks represent water voxels (they point in the same direction as the organ, because the dose should be minimal here), while the downward peaks are connected to the tumor voxels. The graphs of beams 2 and 4 show very clear at which energy the middle of a certain voxel is. The centre of the first voxel is at 32-33 MeV (= 1 cm), and that is the reason why the gradient is zero for lower energy groups, which leads to a non-zero value for the input flux.

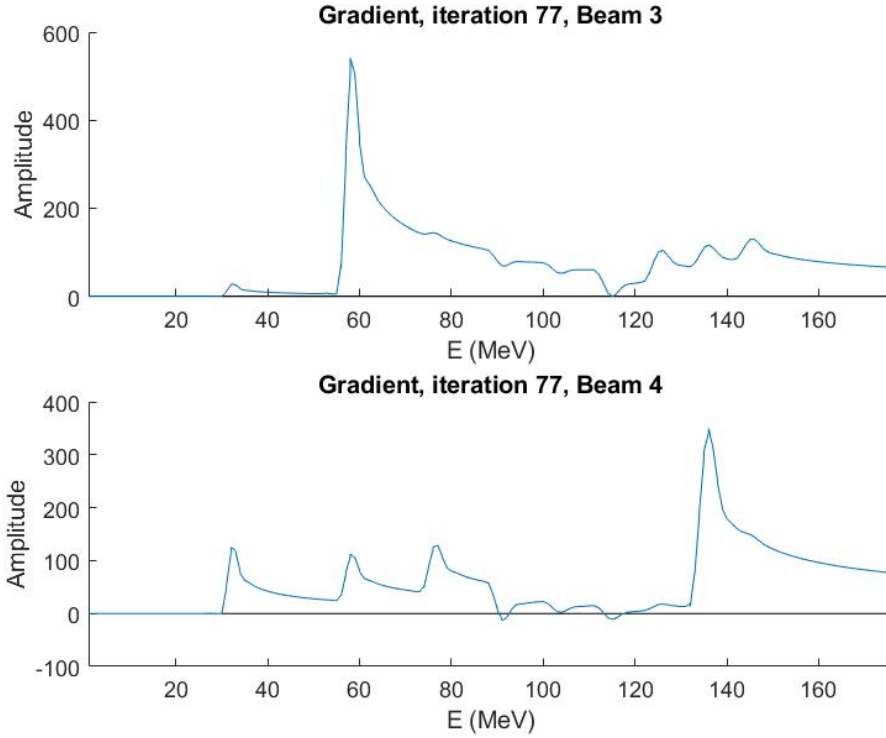


Figure 17: The gradient for beams 3 and 4 at iteration 77. The high peaks represent the location of organ voxels. The smaller upward peaks are connected to water voxels and downward peaks correspond to tumor voxels. The gradient is zero at low energies.

Although the amplitude of the gradient is not zero everywhere, the algorithm converged. The stepsize tolerance is reached and the objective value did not improve. Most likely, the non-negativity constraint avoided to follow the shape of the gradient, when searching for new optimization variables. The input flux at the organ and water locations is already zero (Figures 14 and 15), so a positive gradient does not affect this (the flux cannot become negative). Besides, the gradient is almost zero at the position of the tumor voxels, and only slightly more dose is needed in the tumor voxels. Therefore, no significant improvement in the objective value can be made.

4.6 Influence of direction

In Sections 4.3, 4.4 and 4.5, only two possible beam directions were used: \hat{x} and $-\hat{x}$. To check the influence of more possible beam directions, new direc-

tions were added to the previous ones each time, see Table 3. Normalization of the directions is not needed for the computations.

Table 3: An overview of the beam directions. New directions were added to the previous ones, when increasing the number of directions. Normalization of the directions is not needed for the computations.

Number	Direction
	$+\hat{x}$
2	$-\hat{x}$
	$+\hat{y}$
	$-\hat{y}$
	$+\hat{z}$
6	$-\hat{z}$
	$+\hat{y} + \hat{z}$
	$+\hat{y} - \hat{z}$
	$-\hat{y} + \hat{z}$
10	$-\hat{y} - \hat{z}$
	$+\hat{x} \quad +\hat{z}$
	$+\hat{x} \quad -\hat{z}$
	$-\hat{x} \quad +\hat{z}$
14	$-\hat{x} \quad -\hat{z}$
	$+\hat{x} + \hat{y}$
	$+\hat{x} - \hat{y}$
	$-\hat{x} + \hat{y}$
18	$-\hat{x} - \hat{y}$

The phantom remained the same as before (Section 4.1). All parameters equal the values in Table 1, except the number of energy groups and E_{max} , which are increased to 215 and 216 MeV, respectively, to make sure all beams can cover the entire phantom for every start position and beam direction (= 27.86 cm at most), and to keep the energy group width equal to 1 MeV. Figure 18 shows the results for multiple beam directions.

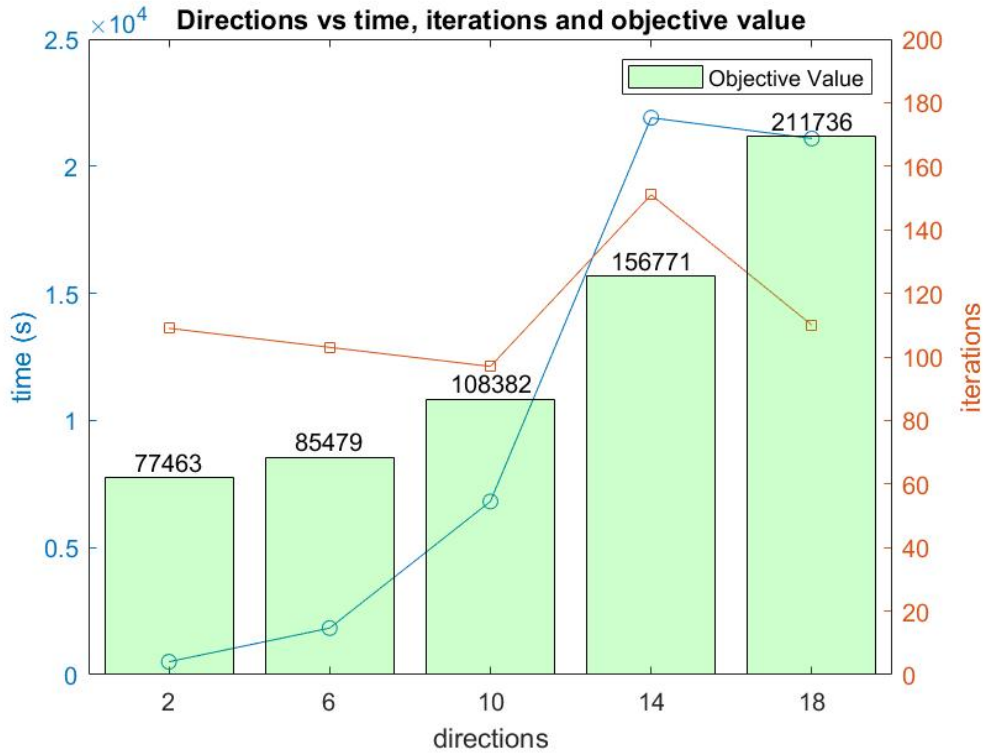


Figure 18: The number of directions versus time, the number of completed iterations and objective value. New directions were added to the previous directions. The time and objective value are increasing with the number of directions. The number of iterations does not follow a specific behaviour. All computations stopped, because the stepsize tolerance was reached and the objective value did not improve.

The computation time increases (exponential) for more possible beam directions. If multiple directions are possible, more calculations have to be done and more beams have to be compared. The number of iterations does not follow a specific behaviour. In every case, the stepsize tolerance limit, $1.0 \cdot 10^{-10}$, is reached and no significant improvement is made, which means a possible local minimum is achieved. Surprisingly, the objective value is increasing for a higher number of directions. The solver has more optimal variables to determine, and might have a harder time to make the best choice (despite using the gradient). For example, the solver can first allow all beams to irradiate the tumor, but then has trouble to set the flux of all beams which do cross organs first to zero. This results in non-zero flux from every direction,

including directions which leads to crossing organs. When more directions are used, a higher objective value is achieved.

5 Conclusion and Recommendations

Conclusions about the results are made in Section 5.1. Recommendations for future research are provided in Section 5.2.

5.1 Conclusion

In this thesis, the accuracy of the adjoint method to choose a selection of optimal beam angles and beam weights for radiotherapy treatment planning is investigated. An iterative algorithm is developed to compute the optimization variables. Adjoint transport and forward transport for protons are performed to obtain the results.

A small and simple 3D phantom is created to test the adjoint method. The selection of optimal beam angles and beam weights is chosen according to a least squares objective function. The flux coefficients for each energy group are determined by a minimum constrained solver.

For two possible beam directions, the final objective value after applying the adjoint method on the set-up case decreased from $1.728 \cdot 10^6$ to $8.12 \cdot 10^4$. 77 iterations and 290 seconds were needed to achieve a possible local minimum. The stepsize tolerance was reached.

The dose distribution, the input flux, and the gradient are investigated as well. All are in agreement with each other. The tumor voxels nearly received the prescribed dose.

The influence of increasing the number of possible beam directions is not clear. An increase in the objective value is noted, while a decrease is expected. The solver might have difficulties in selecting the best beams, if more options are present. However, this needs to be investigated in more detail.

5.2 Recommendations

The adjoint method looks promising to be used in the future. However, the results are not fully representative in reality, since some simplifications are implemented. Therefore, several improvements have to be done, before it is really applicable in practice.

In this research, the proton transport was modelled with the Fokker-Planck approximation, and only the continuous slowing down operator and the straggling operator were included. The accuracy of the adjoint method could be improved, if scatter and diffusion interactions are taken into account as well.

Second, the discretization error for low energy groups has to be solved. This could be done by using a different discretization method or by adjusting the current one. A quick and dirty solution is to use very small voxel sizes or to increase E_{min} . However, that would not solve the actual problem.

The beams have an infinitesimally small width when crossing the phantom, but it includes the area of a side of a voxel when depositing dose. Real pencil beams with a finite width should be implemented to obtain a better physical result. This could also lead to a more uniform dose distribution.

The adjoint approximation has a linear character and higher order terms were neglected in the perturbation analysis. This was done to save computation time, but leads to inaccuracies. Besides, the effect of protons streaming out of the lowest energy group was neglected, which leads to a fraction of non-deposited energy, and therefore a lower dose deposition.

Finally, the algorithm can be expanded for more types of tissues (skin and bone for example), and different input parameters can be tested. Besides, the set-up was very coarse and a decreased voxel size could lead to different insights at smaller scale. For large systems (with a lot more directions and thus optimization variables) with smaller stepsizes, the `fmincon` solver might have trouble finding converging optimal values. The computation time would also increase exponentially, which should be avoided. Furthermore, different types of responses such as the minimum and maximum dose, the tumor control probability and the normal tissue complication probability could be investigated, while using a real CT-scan instead of a simple user-made phantom.

References

- [1] J. J. Duderstadt and L. J. Hamilton, “Nuclear reactor analysis”, *Inc.*, New York, 1976.
- [2] A. Brahme, “Optimization of stationary and moving beam radiation therapy techniques”, *Radiotherapy and Oncology*, vol. 12, no. 2, pp. 129–140, 1988.
- [3] F. C. Difilippo, “Forward and adjoint methods for radiotherapy planning”, *Medical physics*, vol. 25, no. 9, pp. 1702–1710, 1998.
- [4] E. Anderson, Z. Bai, C. Bischof, S. Blackford, J. Demmel, J. Dongarra, J. Du Croz, A. Greenbaum, S. Hammarling, A. McKenney, and D. Sorensen, *LAPACK Users’ Guide*, Third. Philadelphia, PA: Society for Industrial and Applied Mathematics, 1999, ISBN: 0-89871-447-8 (paperback).
- [5] M. E. Kowalok, *Adjoint methods for external beam inverse treatment planning*. University of Wisconsin–Madison, 2004.
- [6] R. A. C. Siochi, *High definition conformal arc radiation therapy with a multi-leaf collimator*, US Patent 6,813,336, Nov. 2004.
- [7] M. Van Herk, “Errors and margins in radiotherapy”, in *Seminars in radiation oncology*, Elsevier, vol. 14, 2004, pp. 52–64.
- [8] T. Bortfeld, “Imrt: A review and preview”, *Physics in Medicine & Biology*, vol. 51, no. 13, R363, 2006.
- [9] B. Rivière, *Discontinuous Galerkin methods for solving elliptic and parabolic equations: theory and implementation*. SIAM, 2008.
- [10] D. Jette and W. Chen, “Creating a spread-out bragg peak in proton beams”, *Physics in Medicine & Biology*, vol. 56, no. 11, N131, 2011.
- [11] P. Van Slingerland and C. Vuik, “Spectral two-level deflation for dg: A preconditioner for cg that does not need symmetry”, 2011.
- [12] S. B. Uilkema, “Proton therapy planning using the sn method with the fokker-planck approximation”, *Delft University of Technology*, 2012.
- [13] H. P. Langtangen, *Introduction to computing with finite difference methods*. University of Oslo, 2013.
- [14] MATLAB, *version 9.4 (R2018a)*. Natick, Massachusetts: The MathWorks Inc., 2018.
- [15] W. Pols, “Working towards a fast prompt gamma emission simulator based on the boltzmann equation”, Master’s thesis, Oct. 2018.
- [16] L. Liao, G. J. Lim, and X. Zhang, “A molecular dynamics approach for optimizing beam intensities in impt treatment planning”, *Journal of Applied Mathematics and Physics*, vol. 7, no. 9, pp. 2130–2047, 2019.

- [17] H. R. Max Roser, *Cancer*, Accessed: 2020-09-29, Nov. 2019. [Online]. Available: <https://ourworldindata.org/cancer#is-the-world-making-progress-against-cancer>.
- [18] T. Burlacu, “Gauging the effect of energy straggling on proton dose distributions”, Master’s thesis, Jan. 2020.
- [19] D. Lathouwers, “Boundary conditions derivation”, internal communication, 2020.
- [20] M. Romme, “Approximating the effects of uncertainties in proton therapy using adjoint theory”, Bachelor’s Thesis, Jul. 2020.
- [21] S. Wendt, “Uncertainty analysis in proton therapy using adjoint theory”, Master’s thesis, Feb. 2020.
- [22] *Cancer statistics*, Accessed: 2020-09-29. [Online]. Available: <https://www.cancer.gov/about-cancer/understanding/statistics#:~:text=Cancer%5C%20is%5C%20among%5C%20the%5C%20leading,related%5C%20deaths%5C%20to%5C%2016.4%5C%20million>.